Summer 2015

Seismological investigation of the Okavango Rift, Botswana

Youqiang Yu

SEISMOLOGICAL INVESTIGATION OF THE OKAVANGO RIFT, BOTSWANA

by

YOUQIANG YU

A DISSERTATION

Presented to the Faculty of the Graduate School of the

MISSOURI UNIVERSITY OF SCIENCE AND TECHNOLOGY

In Partial Fulfillment of the Requirements for the Degree

DOCTOR OF PHILOSOPHY

In

GEOLOGY AND GEOPHYSICS

2015

Approved by:

Stephen Gao, Advisor

Kelly Liu, Co-Advisor

Andreas Eckert

J. David Rogers

Kevin Mickus

PUBLICATION DISSERTATION OPTION

Pages 3-19 were submitted to the Geophysical Journal International; pages 20-43 were submitted to the Earth Planetary Science Letter; pages 44-65 have been published in the Journal of Geophysical Research: Solid Earth.

ABSTRACT

The mechanisms of rifting have been intensively investigated using geological and geophysical techniques beneath mature rift zones. However, current understanding on the earliest stages of rifting is seriously limited. Here we employ recently archived data from 17 broadband seismic stations traversing northern Botswana to conduct the first shear wave splitting and mantle transition zone (MTZ) studies within the Okavango Rift Zone (ORZ). The ORZ is an incipient continental rift situated at the terminal of the southwestern branch of the East African Rift System. The resulting normal MTZ thickness and consistently rift-parallel fast polarizations imply an absence of significant thermal anomalies in the upper mantle, ruling out the role of mantle plumes in the initiation of the ORZ. The observed anisotropy beneath the ORZ and adjacent areas is mainly attributed to the relative movement between the lithosphere and asthenosphere with regional contributions from fabrics in the lithosphere and flow deflection by the bottom of the lithosphere. Our observations imply that the initiation and development of the ORZ can be initiated following a passive mode from the consequences of relative movements between the South African block and the rest of the African plate along a zone of lithospheric weakness between the Congo and Kalahari cratons.

In addition, an approach was developed to effectively remove the near surface reverberations in the resulting receiver functions, decipher the P-to-S converted phases associated with the Moho discontinuity, and thus resolve sub-sediment crustal structure beneath stations sitting on a low-velocity sedimentary layer.

ACKNOWLEDGMENTS

I would like to express my deep appreciation and gratitude to my advisor, Dr. Stephen Gao; co-advisor, Dr. Kelly Liu for the patient guidance and mentorship they provided to me. Dr. Gao shows me how to be an outstanding research scientist in terms of skills on critical thinking, writing, speaking, and teaching. I learned from Dr. Liu what a perfect work will be and the spirit of working hard and carefully, which will benefit my future career.

I would like to thank my committee members, Dr. Andreas Eckert, Dr. David Rogers, and Dr. Kevin Mickus for being my PhD committee members and their constructive suggestions. The financial support from US National Science Foundation and China Scholarship Council are greatly appreciated. I also appreciate the field assistance provided by Dr. Angela M. Reusch from PASSCAL, Dr. Moikwathai Moidaki and student Keletso Kaisara from the University of Botswana, and the local people in Botswana. Patti Adams, Patti Robertson and Paula Cochran from the department of Geosciences and Geological and Petroleum Engineering, gave significant help for the success of my field trips in Botswana from the past two-years. I want to thank the help and suggestions from my friends and colleagues of the geophysics group.

Special thanks to my family for their unwavering support and unceasing encouragement. Words cannot express how grateful I am to my mother and father for all of the sacrifices that they have made on my behalf.

TABLE OF CONTENTS

LIST OF ILLUSTRATIONS

Figure Page

PAPER I

PAPER II

PAPER III

SECTION 2

LIST OF TABLES

NOMENCLATURE

Symbol	Description
PAPER I	
Δ	Epicentral distance
δt	Time residual of teleseismic P and S waves
δ_t^c	Time residual after elevation-correction
PAPER II	
Θ	Fast orientation
δt	Splitting time
PAPER III	
$\delta(t)$	Dirac delta function
r_0	The strength of the near surface reverberations
Δt	The two-way travel-time for the reverberations of the converted waves in the sedimentary layer
$F(t)$	The RF without the influence of the sedimentary layer
$H(t)$	The RF with the influence of the sedimentary layer
H	Candidate thickness
k	Candidate Vp/Vs
ω	Weighting factor

SECTION

1. INTRODUCTION

Rifting of continental lithosphere plays a significant role in the development of continents and the birth of ocean basins. The mechanisms of rifting can be generally divided into active and passive. In the either passive or active scenario, mantle upwelling and melting are all observed at the last stage of rifting (Sengor and Burke, 1978; White and McKenzie, 1989). Thus, it is difficult to distinguish the driving forces of rifting based on the studies from mature rift zones such as Afar Depression, Main Ethiopia Rift, which have been intensively investigated by previous projects. In this study, we conduct the first teleseismic study on the incipient Okavango rift zone (ORZ), intending to decipher the rifting mechanisms at its early stage.

The dissertation is mainly composed of three parts. The first part demonstrates the studies of mantle transition zone (MTZ). The resulting normal MTZ thickness and shallower than normal MTZ discontinuities depths imply the absence of significant thermal anomalies possible existing in the upper mantle beneath the ORZ.

Shear wave splitting analysis is discussed in the second part. The resulting dominant rift parallel fast orientations rule out the existence of upper mantle plume and small-scale convection. The observed seismic anisotropy is possibly induced by the relative movement between the lithosphere and asthenosphere. Based on the analysis of mantle transition zone and shear wave splitting, the Okavango rift can be initiated by intra-plate relative motions of continental blocks along zones of weakness produced by ancient tectonic events.

The third part shows our self-developed technique that can significantly remove the reverberations caused by the surface low-velocity sedimentary layer, decipher the masked P-to-S converted phases generated from the Moho discontinuity in the resulting receiver functions, and is tested to be an efficient tool in resolving the sedimentary and sub-sediment crustal thickness and Vp/Vs.

PAPER

I. NO THERMAL ANOMALIES IN THE MANTLE TRANSITION ZONE BENEATH AN INCIPIENT CONTINENTAL RIFT: EVIDENCE FROM THE FIRST RECEIVER FUNCTION STUDY ACROSS THE OKAVANGO RIFT ZONE, BOTSWANA

Abstract

The Okavango Rift Zone (ORZ) of northern Botswana is an incipient continental rift situated within the Neoproterozoic Damara belt between the Congo Craton to the northwest and the Kalahari Craton to the southeast. Mantle structure and thermal status beneath the ORZ are poorly known, mostly due to a complete paucity of broadband seismic stations in the area. As a component of an interdisciplinary project funded by the United States National Science Foundation, a broadband seismic array was deployed over a 2-year period between mid-2012 and mid-2014 along a profile 750 km in length. Using P-to-S receiver functions (RFs) recorded by the stations, the 410 and 660 km discontinuities (d410 and d660) bordering the mantle transition zone (MTZ) are imaged for the first time. When a standard Earth model is used for the stacking of RFs, the apparent depths of both discontinuities beneath the Kalahari Craton are about 15 km shallower than those beneath the Congo Craton. Using teleseismic P- and S-wave travel-time residuals obtained by this study and lithospheric thickness estimated by previous studies, we conclude that the apparent shallowing is the result of a 100-150 km difference in the thickness of the lithosphere between the two cratons. Relative to the adjacent tectonically stable areas, no significant anomalies in the depth of the MTZ discontinuities or in teleseismic P- and S-wave travel-time residuals are found beneath the ORZ. These

observations imply an absence of significant thermal anomalies in the MTZ and in the upper mantle beneath the incipient rift, ruling out the role of mantle plumes in the initiation of the ORZ. We propose that the initiation and development of the ORZ were the consequences of relative movements between the South African block and the rest of the African plate along a zone of lithospheric weakness between the Congo and Kalahari cratons. An area of thinner-than-normal MTZ is found at the SW corner of the study area. This anomaly, if confirmed by future studies, could suggest significant transferring of heat from the lower to the upper mantle.

1. Introduction

The mechanisms controlling the initiation and development of continental rifting can be generally categorized into active and passive processes, wherein the principle distinction depends upon the driving forces that promote lithospheric extension (Sengor and Burke, 1978). Active rifting is broadly induced by a hot, actively upwelling asthenosphere followed by extensive magmatic diking and regional uplift, while passive rifting demonstrates crustal extension ambiguously accompanied by volcanism or uplift, and is commonly caused by far-field plate driving forces (Sengor and Burke, 1978; White and McKenzie, 1989). Observations on the state of rifting and the geodynamic controls governing their evolution were primarily obtained, however, from relatively mature rift zones such as the Main Ethiopian and Kenyan Rifts of the northernmost East African Rift System (EARS). Meanwhile, the characterization of the initiation and early-stage evolution of continental rifting, exemplified by the southern and southwestern EARS rift

segments such as the Malawi (Ebinger et al., 1984) and Okavango rift zones, is largely underdeveloped.

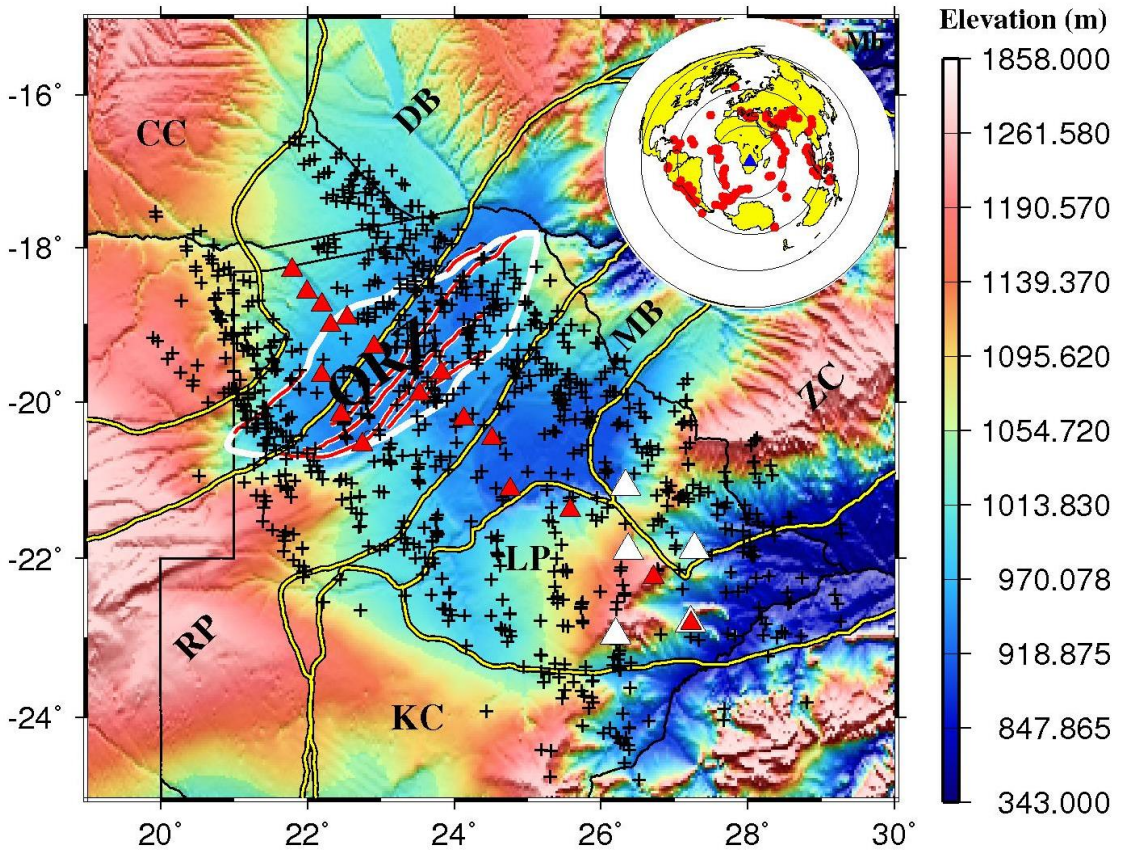

Figure 1. A topographic relief map of the study area showing the SAFARI (red triangles) and SASE (white triangles) seismic stations used in the study. Crosses are ray-piercing points above the depth of 535 km. Red lines show active faults (Kinabo et al., 2008) and yellow lines delineate boundaries of major tectonic units modified from Hanson (2003) and McCourt et al. (2013). CC: Congo Craton, DB: Damara Belt, KC: Kaapvaal Craton, LP: Limpopo Belt, MB: Magondi Belt, ORZ: Okavango Rift Zone, RP: Rehoboth Province, ZC: Zimbabwe Craton. The fan-shaped area is the Okavango Delta. The inset is an azimuthal equidistant projection map centered at the study area, showing the distribution of earthquakes (red dots) used for the receiver function study.

The Okavango Rift Zone (ORZ), located in northern Botswana, is believed to be an incipient rift at the terminus of the southwestern branch of the EARS (Reeves, 1972; Modisi et al., 2000). The ORZ is mainly situated within the Neoproterozoic Damara belt

and the reworked Paleo-Mesoproterozoic crust of the Rehoboth Province, and develops as a transition zone between the Neoproterozoic Congo Craton to the northwest and the composite Archean Kalahari Craton (which, in the study area, includes the Kaapvaal and Zimbabwe cratons and the Limpopo belt) to the east-southeast (Hanson, 2003; Kinabo et al., 2008; Begg et al., 2009) (Figure 1). The Damara Belt is a Pan-African suture formed during East and West Gondwanaland collision, or is a collapsed intracontinental basin (Stern, 1994). It is a major zone of lithospheric weakness in southern Africa, extending from Namibia on the southwestern African coast northeastward into Zambia (Begg et al., 2009).

Surface geological observations and crustal geophysical studies indicate that the ORZ is in its earliest recognizable stage of development, with initiation of rifting estimated to be between 40 and 27 ka (Modisi et al., 2000; Kinabo et al., 2008; Miensopust et al., 2011; Bufford et al., 2012). Due to a complete paucity of broadband seismic stations in the vicinity of the ORZ, the structure and thermal state of the upper mantle and the mantle transition zone (MTZ) have not been investigated with sufficient spatial resolution beneath the incipient rift.

Numerous previous studies suggest that the MTZ, which is confined by seismic discontinuities at approximate depths of 410 km and 660 km (hereafter referred to as d410 and d660, respectively), is sensitive to variations in mantle composition and temperature in the vicinity of the discontinuities. Relatively colder and warmer regions are expected to have thicker and thinner MTZ, respectively, due to their characteristic Clapeyron slopes (positive for d410 and negative for d660) (Bina and Helffrich, 1994). The presence of water in the MTZ can have the same effect as decreasing temperature

and will subsequently thicken the MTZ (Litasov et al., 2005). Hence, variations in MTZ thickness and depths of the MTZ discontinuities can behave as a proxy with which to detect the existence of thermal anomalies and help distinguish the mode of rifting. Such a tool has been applied to other regions of continental rifting. For instance, the Baikal rift was found to have a cold MTZ based on an observed uplifted d410 (Liu and Gao, 2006), and studies in the Rio Grande rift suggested the lack of a large-scale thermal anomaly in the MTZ (Wilson et al., 2005; Gao and Liu, 2014a). Beneath the Kenya and Tanzania segments of the EARS, receiver function (RF) studies revealed a thin MTZ, which was interpreted to be associated with the African superplume (Huerta et al., 2009; Mulibo and Nyblade, 2013). In contrast, beneath southern Africa, Gao et al. (2002) observed a normal MTZ thickness and concluded that the African Superplume, if it exists, is constrained in the lower mantle beneath the study area. This conclusion is supported by the seismic tomography study of James et al. (2001). The present study represents the first seismological investigations of the upper mantle and mantle transition zone beneath the ORZ using broadband seismic data recorded in the vicinity of the rift.

2. Data and Methods

In the summer of 2012, a total of 17 broadband seismic stations were deployed in northern and central Botswana along a NW-SE profile with an average station spacing of 72±34 kilometers (Figure 1), as part of the Seismic Arrays for African Rift Initiation (SAFARI) project (Gao et al., 2013; Yu et al., 2013). The 17 SAFARI broadband stations, which were equipped with Quanterra Q330 digitizers and Guralp CMG-3T 120 s sensors, recorded continuously with a sampling rate of 50 Hz until the summer of 2014.

Additionally, data from 5 broad-band seismic stations from the 1997-99 Southern African Seismic Experiment (SASE) (Gao et al., 2002) are used to enhance coverage and resolution of our data set (Figure 1). Data from events in the epicentral distance range of 30 to 100° are selected with a cut-off magnitude of Mc as defined by $Mc = 5.2 + \frac{\Delta - 30.0}{180.0 - 30.0} - D/700.0$, where Δ is the epicentral distance in degree and D is the focal depth in km (Liu and Gao, 2010). Such an empirical formula was designed to balance the quantity and quality of the data to be processed.

2.1 Receiver Function Stacking

The original seismograms are windowed 20 s before and 260 s after the first P arrival and are bandpass filtered with a four-pole, two-pass filter in the frequency range of 0.02-0.2 Hz. The filtered seismograms with signal-to-noise ratios (SNR) exceeding 4 on the vertical component are converted into radial RFs using the procedure of Ammon (1991). A set of exponential functions are adopted to minimize the degenerating effects of the PP arrivals on the RFs (Gao and Liu, 2014b). The resulting RFs are subsequently subjected to a SNR-based procedure to select the high quality RFs (see Gao and Liu, 2014a for more information about the specific definition of the SNR and details of the procedure). A total of 1064 high-quality RFs from 22 seismic stations and 159 teleseismic events are obtained (Figure 1).

The geographic coordinates of the ray-piercing points for each of the selected RFs are computed at approximately the middle of the MTZ (535 km) using the IASP91 Earth model. Based on the locations of the ray-piercing points, we group the RFs into circles with a radius of 1°. The circles are aligned along the latitudinal and longitudinal lines with a separation of one geographic degree between adjacent circles. The RFs in a given

circle are then moveout corrected and stacked for the depth range of 350-700 km with a vertical resolution of 1 km, under a non-plane wave assumption (Gao and Liu, 2014b). Because a 1-D Earth model is used for the migration and stacking of the RFs, the observed MTZ discontinuity depths are apparent rather than true depths. The stacked depth series are visually checked to ensure quality. A bootstrap resampling approach with 50 resampling iterations (Efron and Tibshirani, 1986) is applied to obtain the mean and standard deviation (SD) of the MTZ discontinuity depths (Liu et al., 2003).

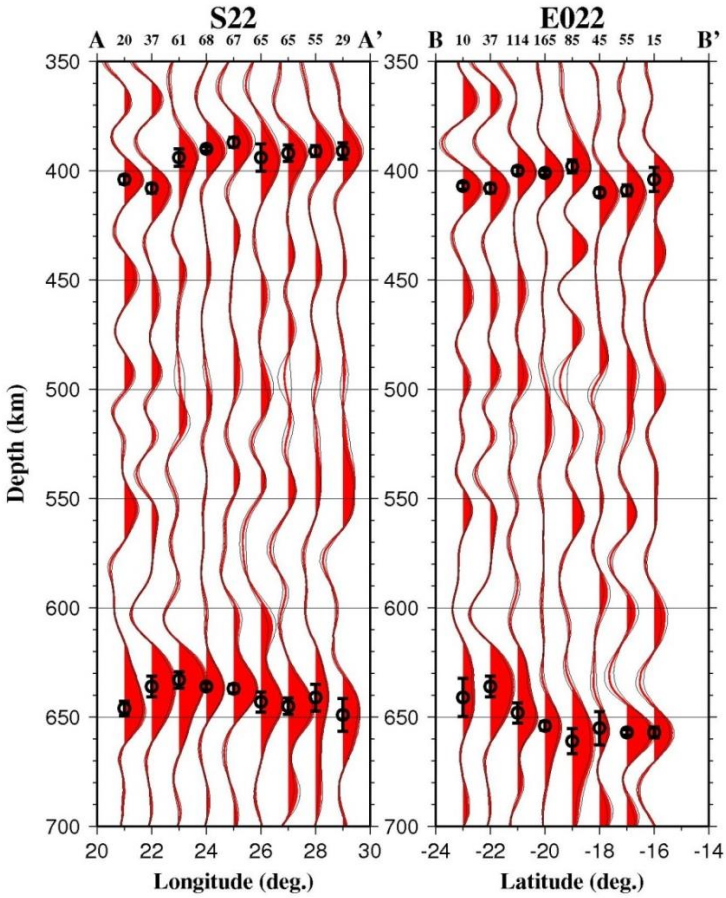

Figure 2. Example depth series from stacking of RFs in radius=1° circles along E-W (left) and N-S (right) profiles (see Figure 4a for locations). The thick red lines show the mean depth series averaged over all the 50 bootstrap iterations, and the bordering thin black lines show the mean ± the standard deviation. The circles with error bars are the average depths of the d410 and d660. The number on the top of each trace represents the number of RFs in the circle.

Figure 2 shows examples of resulting depth series along two profiles. Note that the existence of lateral variations in the velocity structure can reduce the stacking amplitude and broaden the peak at the estimated MTZ discontinuity depths (Mohamed et al., 2014). In addition, the stacking results near the edges of the study area are not as reliable as those in the interior due to the lower number of RFs.

2.2 Travel-Time Residuals

Both thermal anomalies in the vicinity of and velocity undulations above the MTZ discontinuities can lead to observed variations in the depths of the discontinuities. In order to provide constraints on the interpretation of the resulting MTZ discontinuity depths, we also measured P- and S-wave travel-time residuals. P- and S-wave arrivals relative to the IASP91 Earth model are manually picked on the vertical and transverse components, respectively, and the mean residual from the event is removed to obtain relative travel-time residuals. Events recorded by less than 5 stations are not used.

We use the following equation to correct for travel-times due to variations in station elevation

$$\delta t_{ij}^{c} = \delta t_{ij} - \frac{h_i}{v \times cos(asin(R_{ij} \times v))} \quad (1)$$

where h_i is the elevation (in km) for the ith station, δt_{ij} is the original residual (in seconds) observed at the ith station from the jth event, R_{ij} is the ray parameter (in s/km), and v is the average velocity (in km/s) in the layer above sea-level. In this study we use 5.5 km/s for P-wave, and $5.5/\sqrt{3}$ km/s for S-wave velocities.

3. Results

3.1 Apparent Discontinuity Depths and MTZ Thickness

A total of 53 circles with clearly observable d410 or d660 arrivals are obtained from our data set. Amongst these circles, 53 of them possess identifiable d410 arrivals and 50 have reliable d660 arrivals. All of the 53 depth series plotted along 9 latitudinal lines (from 16°S to 24°S with an increment of 1°) are shown in Figure 3. To produce spatially continuous images for the observed depths and MTZ thickness, we fit the observations using a continuous curvature surface gridding algorithm, with a tension factor of 0.5 (Smith and Wessel, 1990) (Figure 4). For the majority of the study area, the SD of the resulting MTZ thickness is less than 5 km (Figure 4d).

The mean apparent depth of d410 for the entire study area is 398±6 km, that of d660 is 646±7 km, and the average MTZ thickness is 248±6 km which is almost identical to the normal thickness of 250 km in the IASP91 Earth model. The apparent depths of both d410 and d660 decrease systematically toward the southeast, from approximately 410 km and 660 km beneath the NW end to 395 km and 645 km near the SE extreme of the study area (Figure 4). The depths beneath the former area (Congo Craton) are identical to those in the IASP91 Earth model, and those beneath the latter (Kalahari Craton in southern Botswana) are about 15 km shallower, an observation that is consistent with the study of Gao et al. (2002) for southern Botswana.

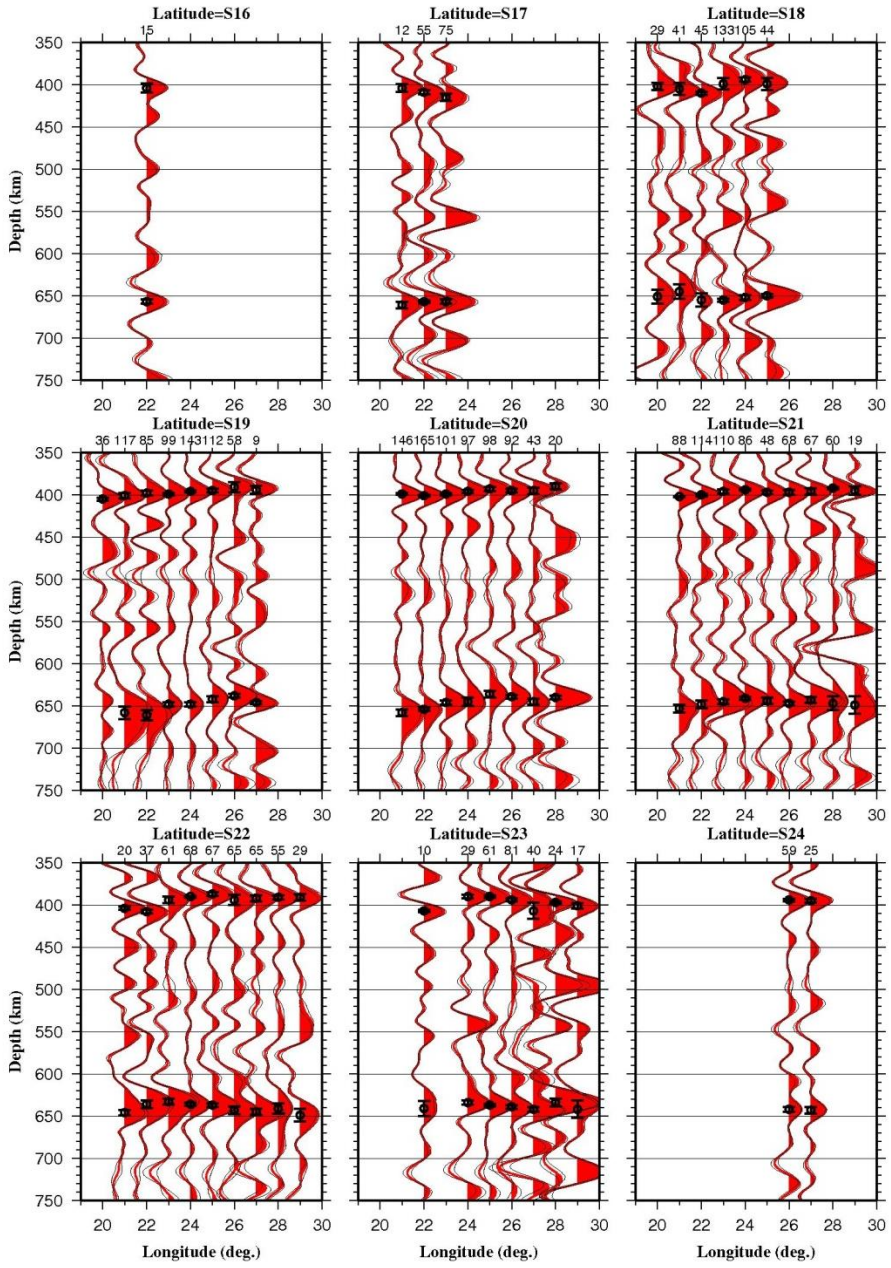

Figure 3.. Same as the previous figure but for all the 9 latitudinal profiles.

The results show that, relative to the immediate adjacent areas, the ORZ displays no observable anomalies in either the apparent depths of the discontinuities or the resulting MTZ thickness. An area of anomalously thin MTZ is observed on the SW corner of the study area, approximately centered at (22°E, 22°S). The anomaly is caused by both a depressed d410 and an uplifted d660, relative to the immediate surrounding

areas (Figure 2). This anomaly, if confirmed, could suggest significant transferring of heat from the lower to the upper mantle beneath western Botswana. Unfortunately, this area is located on the edge of the region sampled by a limited number of RFs (Figure 1). Obviously, additional broadband stations need to be deployed in western Botswana and perhaps eastern Namibia in order to test the existence of such a potentially important feature, which, if confirmed, could have important implications about heat transfer from the lower to the upper mantle. Such a transfer might be related to the African superplume, which is thought to be confined in the lower mantle beneath southern Africa (James et al., 2001; Gao et al., 2002).

3.2 Body-Wave Travel-Time Residuals

We have hand-picked 1832 P- and 1356 S-wave residuals from 172 teleseismic events. The residuals are displayed using different approaches. In Figures 5a and 5b, station averages with standard deviations are displayed along a profile orthogonal to the strike of the ORZ. Such an approach implies that the anomalies in the residuals originate near the surface, which is unlikely. To more reasonably represent the observations, the residuals from individual station-event pairs are displayed at the ray-piercing point at the depth of 100 km, which is approximately the center of the lithosphere in the study area (Muller et al., 2009). The residuals are then projected to a NW-SE oriented profile (Figures 5a and 5b), and are also plotted as images (Figures 5c and 5d).

Both the P- and S-wave travel-time residuals decrease toward the SE. The spatially-averaged residuals have a peak-to-peak magnitude of about 0.6 s for P- and 1.8 s for S-waves (Figure 5). The SE boundary of the ORZ marks the NW end of a linear increase of the travel-time residuals (especially for S-waves). Nevertheless, significant

travel-time delays are not observed in the ORZ, which is in sharp contrast with other continental rift zones. For instance, across the Baikal rift zone, which was similarly developed along the edge of a stable craton (the Siberia Craton), a P-wave travel-time delay as large as 1 s relative to surrounding areas was observed (Gao et al., 2003).

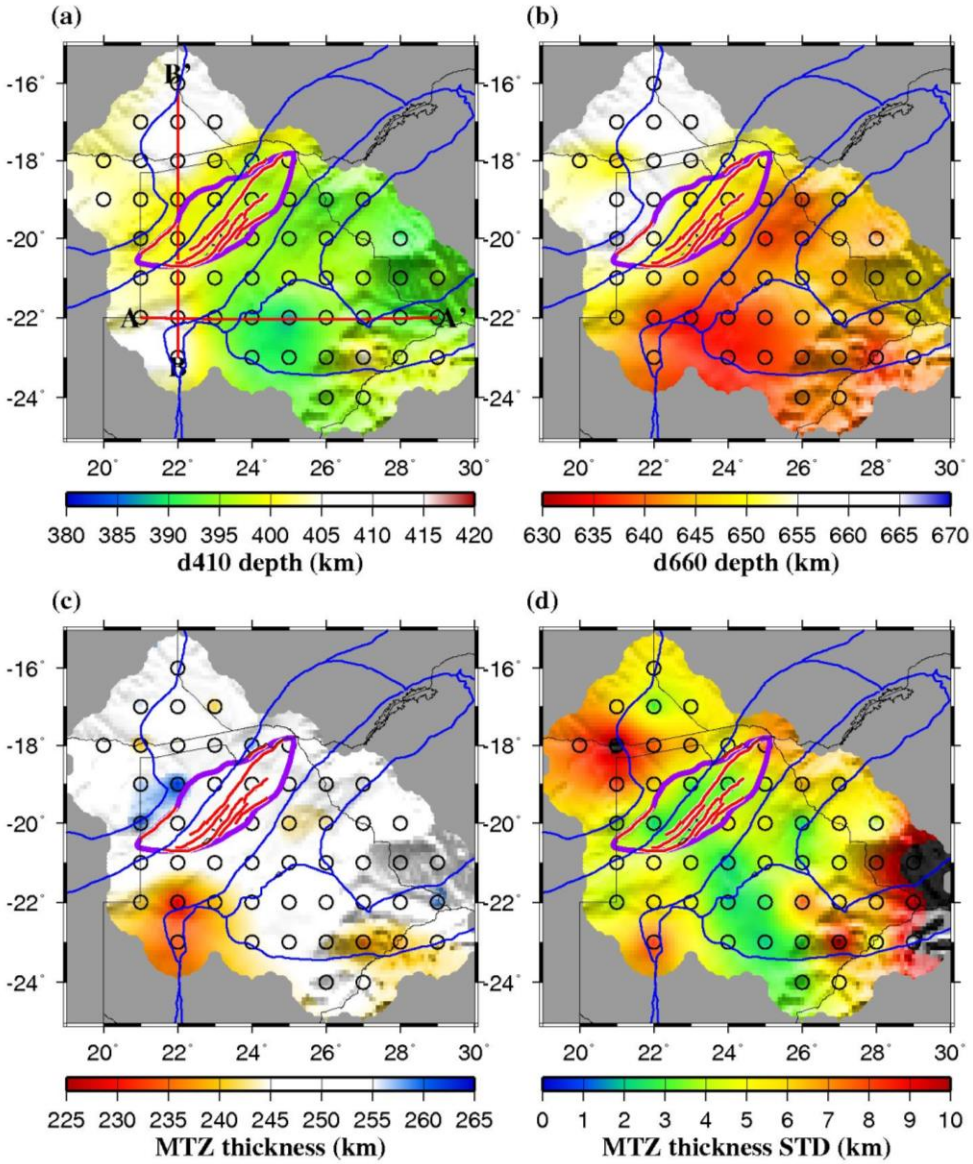

Figure 4. (a) Smoothed spatial distribution of resulting d410 depth; (b) Same as (a) but for d660; (c) MTZ thickness; and (d) Standard deviations of the MTZ thickness measurements. Circles indicate the center of circular areas with high-quality measurements. Note that in (a)-(c), only measurements that are 5 or more km different from the corresponding global average are colored. Profiles A-A' and B-B' in (a) indicate the location of the cross-sections shown in Figure 2.

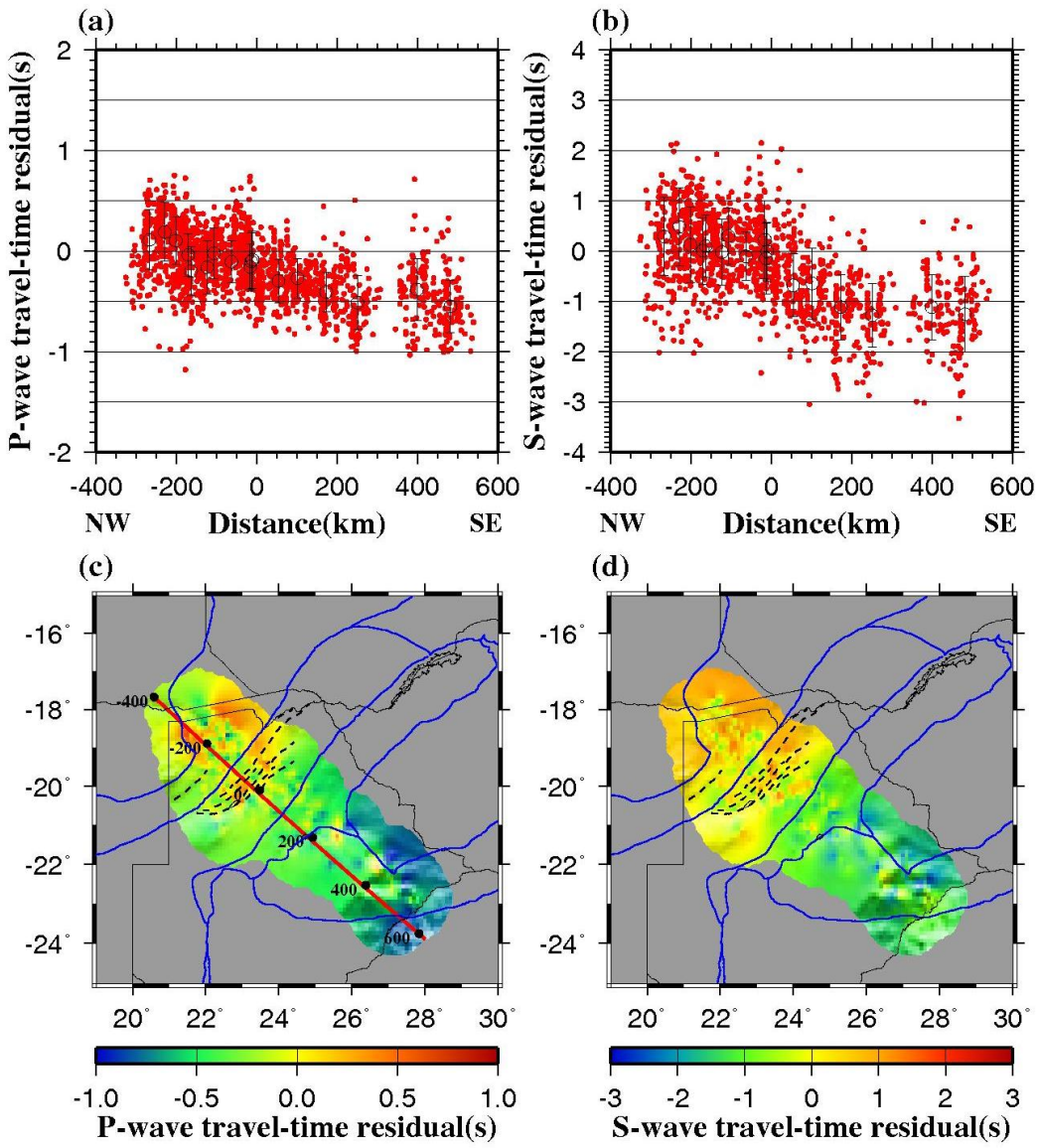

Figure 5. Teleseismic P- and S-wave travel-time residuals displayed above the ray-piercing points at 100 km depth. (a) P-wave residuals projected on to the profile shown in (c). Dots are individual event values, and circles with error bars are station-averaged values. (b) Same as (a) but for S-wave residuals. (c) Spatial distribution of P-wave residuals. (d) Spatial distribution of S-wave residuals.

4. Discussion

4.1 Causes of the Apparent MTZ Depth Variations

To the first-order, the apparent depths of the d410 and d660 (Figure 4) as well as the P- and S-wave travel-time residuals (Figure 5) decrease from the Congo to the

Kalahari cratons. The fact that the MTZ thickness remains the same throughout most of the study area suggests that the apparent variations of the observed depths are mainly caused by lateral velocity variations in the upper mantle, probably by variations in the thickness of the lithosphere. In the following we attempt to test this hypothesis by using the observations obtained in this study and lithospheric thickness estimated from previous studies (James et al., 2001; Muller et al., 2009).

As discussed above, relative to the Congo craton, both the d410 and d660 beneath the Kalahari Craton are uplifted by about 15 km. Under the assumption that this apparent uplift is purely caused by velocity anomalies, we estimate that a 15 km uplift corresponds to a Vp anomaly of +1.2% in the depth range of 0-410 km using the approach of Gao and Liu (2014b). If the anomalous zone is limited in a 100 km thick layer, the required anomaly is about 5%, and this value reduces to about 3% if the thickness is 150 km. In addition, the velocity anomalies resulting in a 15 km apparent uplift of both the d410 and d660 can produce a P-wave travel-time residual of about -0.6 s, which is almost exactly what was observed (Figure 5). To estimate the predicted S-wave travel-time residual using the apparent depression of the discontinuities, the γ value, which is the ratio between S- and P-wave relative velocity anomalies, i.e., $\gamma = dln(V_S)/dln(V_P)$, is required. Under the assumption of $\gamma = 1.7$ which is the same as that found for the stable central and eastern United States (Gao and Liu, 2014a), the predicted S-wave travel-time residual is -1.8 s which is once again consistent with the observed value (Figure 5).

We next explore the possibility that the observed velocity anomalies originate from lateral variations of lithospheric thickness beneath the study area. Seismic tomography studies indicated that the Kalahari cratonic root extends to at least 250 km

and perhaps as deep as 300 km (James et al., 2001). On the other hand, Muller et al. (2009) found that the lithospheric thickness in the vicinity of the Damara belt in the ORZ to be approximately 160 km. These studies suggest that beneath the Kalahari Craton, the lithosphere is approximately 100-150 km thicker than that beneath the northwestern part of the study area. If we assume that this 100-150 km excessive lithospheric thickness is solely responsible for the observed 15 km apparent uplift of the MTZ discontinuities and variations in travel-time residuals, the required P-wave velocity contrast is 3-5% between the lithosphere and the asthenosphere. Velocity contrasts of similar magnitude are commonly found in numerous previous seismic tomography and receiver function studies (e.g., Gao et al., 2003; Rychert et al., 2007).

4.2 Implications for Rifting Mechanisms

The observed normal MTZ thickness, lack of significant travel-time residuals, and absence of elevated mantle conductivity (Khoza et al., 2013) associated with the incipient ORZ suggest the absence of high-temperature anomalies in both the MTZ and the upper mantle, ruling out contributions of one or more mantle plumes in rift initiation and favoring a “passive” origin.

A recent geodetic study (Malservisi et al., 2013) suggested that with respect to the African continent, the rigid South African block rotates clockwise, probably along the Damara belt. Such differential movements between relatively rigid tectonic blocks can rupture the pre-existing weak zones along edges of the blocks. The fractures can then propagate downward through the lithosphere without mantle upwelling anomalies, and rifting processes continue as long as the regional dominant stresses are extensional. A likely environment for reactivation of shear zones adjacent to the ORZ is the

transcontinental Mwembeshi dislocation zone which experiences left-lateral transtension as the consequence of differential extension between Nubia and Somalia (Daly et al., 1989). The Mwembeshi shear zone, which intersects the Luangwa and Malawi rift zones farther to the northeast of the ORZ, has been suggested to exert geometrical control on rift basin development within the EARS (Versfelt and Rosendahl, 1989). Similar lithospheric-scale Proterozoic suture shear zones have been cited as a possible origin for the Kenya Rift (Birt et al., 1997). Differential movements between tectonic blocks in a relatively stable tectonic plate can originate from many factors, such as differences in the direction and/or strength of mantle flow (either as driving or resistant forces), uneven distribution of ridge push and slab pull forces across the plate, spatially varying far-field stress from continental collision, and non-uniform influence of mantle upwelling or down welling (Doglioni, 1993). We speculate that for the ORZ, variations of lithospheric thickness combined with the presence of previously ruptured lithosphere give rise to one or more of the above heterogeneities, leading to rift initiation. This model could explain why most of the world's continental rifts developed along the edges of cratonic blocks, where rapid changes of lithospheric thickness are commonly found (Keller et al., 1991).

5. Conclusion

This first receiver function study of mantle transition zone discontinuities even conducted in the vicinity of the incipient ORZ reveals a normal MTZ temperature beneath most of the study area. The apparently shallower-than-normal MTZ discontinuities observed beneath the Kalahari Craton can be explained by the existence of a lithosphere that is 100-150 km thicker than that beneath the Congo Craton and the

Damara belt. In addition, the ORZ is not associated with significant delays in teleseismic P- and S-wave travel-time residuals, implying the absence of significant mantle anomalies beneath the ORZ. These observations are inconsistent with the existence of mantle plumes or a broadly upwarped asthenosphere beneath the study area. Instead, they provide unprecedented supporting evidence for a model of rift initiation involving lithospheric fracturing due to differential movements between tectonic blocks along pre-existing zones of weakness such as edges of cratonic blocks.

II. SEISMIC ANISOTROPY BENEATH THE INCIPIENT OKAVANGO RIFT: IMPLICATIONS FOR RIFTING INITIATION

Abstract

This study represents the first shear-wave splitting investigation of the Okavango rift zone (ORZ), an incipient continental rift belonging to the East African rift system in northern Botswana. Analysis of broadband seismic data recorded along a 750 km long profile of 22 stations traversing the ORZ and adjacent Congo and Kalahari cratons and several Precambrian orogenic zones reveals dominantly NE-SW fast orientations, which are parallel to both the absolute plate motion direction (based on the NUVEL-1A model) and the trend of most tectonic boundaries, including that of the ORZ. Spatial coherence analysis of the splitting parameters and correspondence between the observed fast orientations and the trend of tectonic features indicate that the main source of observed anisotropy is most likely in the upper asthenosphere, probably due to simple shear associated with the relative movement of the lithosphere against the asthenosphere. The presence of consistently rift-parallel fast orientations and normal splitting times in the ORZ and most parts of southern Africa implies that neither an upper mantle plume nor small-scale convection is the dominant source for rift initiation and development. Our preferred model of continental rupture involves intra-plate relative movement of continental blocks along zones of weakness produced by ancient tectonic events.

1. Introduction

Continental rifting constitutes the transition from stable continental lithosphere into an ocean basin. Numerous studies suggested that continental rifting is either induced

by active mantle upwelling associated with deep mantle plumes (active rifting), or by horizontal motion of plates and their interaction along plate boundaries (passive rifting; Sengor and Burke, 1978; Hill, 1991). These contrasting models of continental rupture are primarily assembled from observations of mature rift zones. In contrast, knowledge of rifting mechanisms and the associated characteristic lithospheric and asthenospheric structure and dynamics beneath incipient rift zones, such as the Okavango rift zone (ORZ) in northern Botswana, is severely limited.

The ORZ (Fig. 1) is one of the youngest continental rifts in the world with an estimated initiation of surface rupture between 120 and 40 ka (Kinabo et al., 2008; Leseane et al., 2015) and thus is an ideal locale to study the characteristics of earliest-stage rifting mechanisms. Situated at the southwestern terminal of the East African rift system (EARS), the ORZ is superimposed upon the Neoproterozoic Damara and Rehoboth orogenic belts (McCourt et al., 2013), which are bounded toward the northwest and southeast by the Congo and Kalahari cratons, respectively (Begg et al., 2009). The latter is a composite terrane composed largely of the Archean Kaapvaal and Zimbabwe cratons and the Archean Limpopo belt. It is encircled by the Paleo- to Mesoproterozoic Namaqua-Natal belt to the south and the Paleoproterozoic Magondi belt and Rehoboth province toward the west (McCourt et al., 2013) (Fig. 1).

While the crustal and mantle structure and dynamics of the Kalahari craton and the mature sections of the EARS have been extensively studied through numerous projects over the past 40 years, the ORZ has not been investigated using robust structural seismological techniques. One such technique is shear-wave splitting (SWS) analysis. It has long been recognized that near-vertically incident shear waves propagating in a

transversely isotropic medium split into two waves with orthogonal polarization orientations (Crampin, 1981). SWS analysis is commonly employed to quantify in-situ lithospheric and asthenospheric seismic anisotropy (e.g., Silver and Chan, 1991). It uses P-to-S converted phases at the core-mantle boundary, including PKS, SKKS, and SKS (which are collectively called XKS), to obtain the two splitting parameters, including the polarization orientation of the fast component (fast orientation or θ), and the splitting time between the fast and slow components (splitting time or δt). The former is an indicator of the orientation of the anisotropic structure, and the latter measures the strength of anisotropy integrated over the whole raypath from the core-mantle boundary to the recording station.

Seismological and petrophysical studies (e.g., Silver, 1996; Gung et al., 2003) have indicated that the dominant contribution to splitting parameters lies primarily within the upper mantle. Several mechanisms have been postulated to produce observed tectonic-scale observable anisotropy. Based upon the strong correlation between splitting parameters and surficial geologic features, seismic anisotropy has been proposed to exist in the lithosphere due to fabrics generated by vertically-coherent lithospheric deformation (Silver, 1996; Silver et al., 2001), or lithosphere-scale magmatic dikes (Gao et al., 1997; Kendall et al., 2006). Alternatively, seismic anisotropy may be induced by present-day upper-mantle flow either as a consequence of simple shear between the rigid lithosphere and mobile asthenosphere, which in turn would produce anisotropy parallel to the absolute plate motion (APM), if the direction of the shear is the same as the APM direction (e.g., Vinnik et al., 1996; Barruol and Ismail, 2001; Gao et al., 2010; Lemnifi et al., 2015), or by small-scale mantle convection (e.g., Gao et al., 1994; Koch et al., 2012).

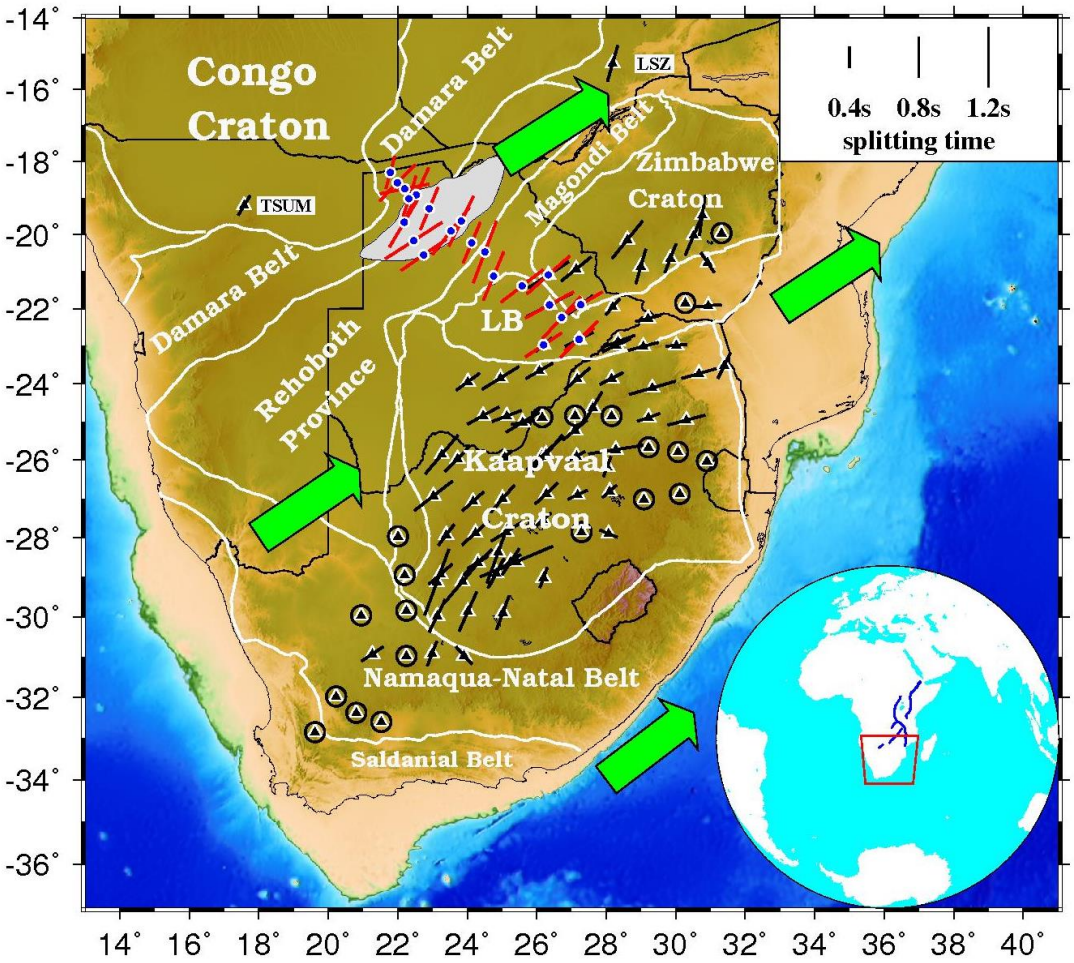

Figure 1. A topographic map of southern Africa showing the major tectonic provinces and station-averaged shear wave splitting measurements from this (blue dots and red bars) and previous (black triangles and bars) studies (Vinnik et al., 1996; Barruol and Ismail, 2001; Silver et al., 2001). Black circles represent null measurements. The Okavango rift zone is highlighted by the grey infilled area. Green arrows represent the APM direction based on the NUVEL-1A model (DeMets et al., 1994). Major tectonic boundaries are plotted as white lines modified from McCourt et al. (2013). LB: Limpopo belt. Note that the Kaapvaal and Zimbabwe cratons and the Limpopo belt are components of the Kalahari craton. The inset shows the location of southern Africa indicated by the red rectangle and the blue lines represent the rift axes of the East African rift system.

SWS studies have been widely conducted in numerous regions of continental rifting affinities. Consistently rift-parallel fast orientations and splitting times substantially larger than the global average of 1.0 s (Silver, 1996) were obtained for the Afar and Main Ethiopian (Gashawbeza et al., 2004; Kendall et al., 2006; Gao et al., 2010),

eastern African (Bagley and Nyblade, 2013), Rio Grande (Sandvol et al., 1992; Liu et al., 2009, 2014; Refayee et al., 2014; Yang et al., 2014), and Baikal (Gao et al., 1997) rifts. Such rift-parallel anisotropy has been attributed to a number of mechanisms, including rift-parallel mantle flow (Sandvol et al., 1992; Gao et al., 2010; Bagley and Nyblade, 2013), lithospheric fabrics formed by past tectonic events (Gashawbeza et al., 2004), and rift-parallel lithospheric dikes (Gao et al., 1997; Kendall et al., 2006). Rift-orthogonal anisotropy observed in the flanking area of the Baikal rift was hypothesized as reflecting the horizontal branches of a small-scale mantle convection system (Gao et al., 1994; 1997).

In general, most modern continental rift zones are associated with rift-parallel fast orientations. Major exceptions to this observation include the Baikal rift zone and the Red Sea which has partially transitioned into an oceanic spreading center. Recent SWS studies (Elsheikh et al., 2014; Lemnifi et al., 2015) in northern Africa and Arabia revealed N-S fast orientations on both sides of the Red Sea, which has a nearly NW-SE strike. Such N-S orientated anisotropy observed in northern Africa and Arabia was proposed to be the result of simple shear developed in the boundary layer between the lithosphere and the asthenosphere formed by long-term northward motion of the African plate relative to the asthenosphere (Elsheikh et al., 2014; Lemnifi et al., 2015).

Splitting measurements are absent in the vicinity of the ORZ due to the heretofore paucity of broadband seismic data. Previous measurements in southern Africa were concentrated on the Kaapvaal and Zimbabwe cratons and the Limpopo belt (Fig. 1). An investigation by Vinnik et al. (1996) at 7 stations on the Kaapvaal craton revealed NE-SW oriented fast orientations, which are parallel to the APM direction of Africa since

Jurassic computed based on the NUVEL-1A model (DeMets et al., 1994), and were therefore interpreted to be the result of APM induced asthenospheric flow. Subsequently, Silver et al. (2001) used a much larger data set recorded at 79 sites in southern Africa and proposed that the observed anisotropy is the result of vertically-coherent lithospheric deformation. Surface-wave studies beneath southern Africa suggested that azimuthal anisotropy varies with depth, implying the presence of anisotropy both in the lithosphere and asthenosphere (Adam and Lebedev, 2012).

This study is part of a multi-disciplinary investigation of the incipient segments of the EARS (Gao et al., 2013). Our main objective is to present results from the first examination of mantle anisotropy using SWS in the vicinity of the ORZ in order to provide constraints on models of rift initiation and anisotropy formation. In doing so, we explore possible relationships between the observed anisotropy with predicted directions of rifting-related mantle flow, the direction of present-day plate motion, and the dominant trend of Precambrian tectonic boundaries.

2. Data and Methods

The broadband seismic data used in the study were recorded by 17 Seismic Arrays for African Rift Initiation (SAFARI) stations that we installed and operated for a two-year period starting from the summer of 2012 (Gao et al., 2013). Data recorded by five stations belonging to the 1997-99 Southern African Seismic Experiment (SASE; Silver et al., 2001) situated immediately within our study area are also used. One of the SAFARI stations, B1665, is located about 1 km away from SASE station SA65 (Fig. 2). The total length of the profile is about 750 km (Figs. 1 and 2). XKS waveforms were

requested from the Incorporated Research Institutions for Seismology (IRIS) Data Management Center (DMC). The epicentral distance range for PKS, SKKS, and SKS is 120-180°, 95-180° and 84-180°, respectively (Liu and Gao, 2013). We apply a cutoff magnitude of 5.6 for events shallower than 100 km while allow for magnitudes from deeper events as low as 5.5 for the purpose of taking advantage of sharper waveforms.

To identify and correct for possible sensor misorientation, we apply the technique developed by Niu and Li (2011) to minimize the P-wave energy on the transverse component. We begin by manually picking the first arrival of the direct P-phase on the vertical component for events recorded by no fewer than 5 stations. The optimal orientation of the N-S component corresponding to the minimum P-wave energy on the transverse component is found using a grid-search algorithm, and is subsequently used to correct for station orientation prior to SWS analysis.

SWS parameters were calculated using the procedure of Liu and Gao (2013) which was based on the method of minimization of transverse energy (Silver and Chan, 1991). The seismograms were first windowed to include the theoretical arrival of the individual XKS phases and then enhanced by applying a band-pass filter with corner frequencies of 0.04-0.5 Hz. All the SWS measurements were visually verified and, if necessary, various adjustments were applied to the beginning and end times of the XKS window, quality ranking, and/or band-pass filtering frequencies to ensure reliability (Liu and Gao, 2013).

Following the evaluation criteria of Liu et al. (2008), we ranked well-defined splitting measurements as either A (outstanding) or B (good) for use in the following SWS analyses. We also analyzed the data set for null measurements, which are

characterized by a lack of observable energy on the transverse component concurrent with a strong XKS arrival on the radial component. Situations wherein the backazimuth (BAZ) is parallel or perpendicular to the fast orientation, or the sub-station crust and mantle are isotropic, can all result in null measurements (Silver and Chan, 1991; Liu and Gao, 2013). As shown in Fig. 2, well-defined splitting parameters were observed at all stations in the study area, suggesting the existence of pervasive anisotropy. Consequently, null measurements will not be discussed below.

3. Results

3.1 Sensor orientation correction

Table 1 shows the optimal orientation of the N-S component of the 3-component sensor for each of the 22 stations. The magnitude of the orientation ranges from -16 to 5° clockwise from the north, with a simple mean of -3±1°. The overwhelmingly negative values of the resulting orientation were most likely the consequences of inadequate correction of the declination of the geomagnetic field, which is about -9° in the study area.

After the application of station orientation correction, the quality of the resulting SWS measurements at stations with misoriented sensors is noticeably improved. Fig. 3 shows an example of the improvement for station B07DX. When the uncorrected data are used for SWS analysis, remaining XKS energy on the corrected transverse seismogram is observable, and the match between the fast and slow components is poor and is accompanied by weak linearity of the corrected particle motion (Fig. 3a). All of these features are indicators of sensor misorientation, as discussed in Liu et al. (2008). The post orientation correction measurement is substantially improved in terms of the removal of

transverse energy, the matching of the fast and slow waveforms, and the linearity of the particle motions (Fig. 3b).

Table 1. Resulting orientation of the N-S component

Station			AZ	No.
Name	Lat.	Lon.		
	deg.	deg.	deg.	events
B01KR	-22.238	26.718	-1	102
B02LT	-21.393	25.581	2	125
B03SL	-21.121	24.764	-6	135
B04KH	-20.474	24.514	-2	125
B05MO	-20.218	24.132	-6	131
B06OR	-19.901	23.527	-10	155
B07DX	-20.549	22.749	-11	115
B08TS	-20.164	22.459	0	84
B09NK	-19.663	22.194	-16	114
B10PP	-18.913	22.543	5	118
B11ET	-19.016	22.316	-1	112
B12SS	-18.746	22.197	3	108
B13NX	-18.579	21.994	4	100
B14MH	-18.295	21.792	-4	117
B15MW	-19.631	23.827	-9	97
B1665	-22.825	27.229	-4	130
B17CI	-19.294	22.909	-13	50
SA64	-22.969	26.202	3	34
SA65	-22.818	27.222	2	39
SA66	-21.900	26.373	-3	38
SA67	-21.886	27.274	-1	35
SA70	-21.088	26.335	-4	41

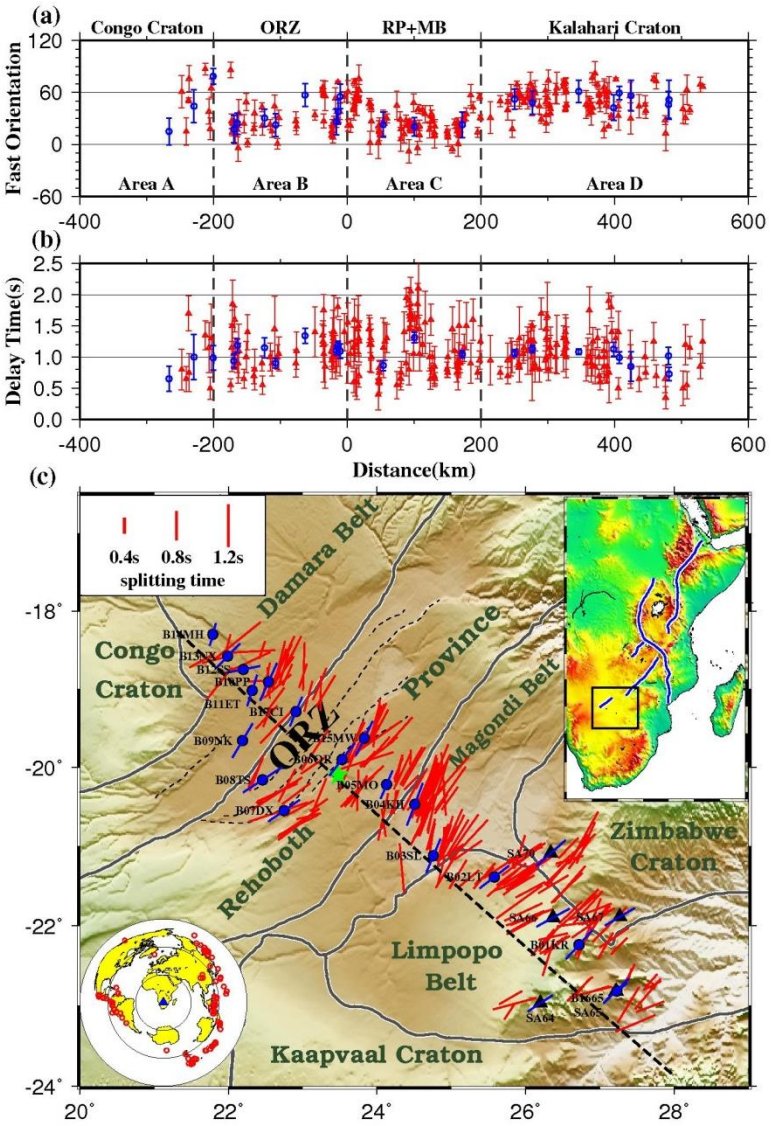

Figure 2. Cross-section and map views of the resulting splitting parameters. (a) Fast orientations projected to the thick dashed profile in (c). Blue bars represent the station-averaged values of the fast orientation while the red bars indicate each individual measurement. RP: Rehoboth province; MB: Magondi belt. (b) Same as (a) but for splitting times. (c) Individual splitting parameters (red) plotted at the 200 km depth ray-piercing points, and station-averaged parameters (blue) plotted at the location of the stations. Grey lines delineate the tectonic provinces, and thin dashed lines within the ORZ area show active faults (Kinabo et al., 2008). SAFARI stations are shown as blue dots and SASE ones as black triangles. The inset in the upper-right corner displays the location of the study area while the one in the lower-left corner shows the distribution of earthquakes (red circles) used in the study. The green star near the SE border of the ORZ marks origin point (zero distance) in (a) and (b).

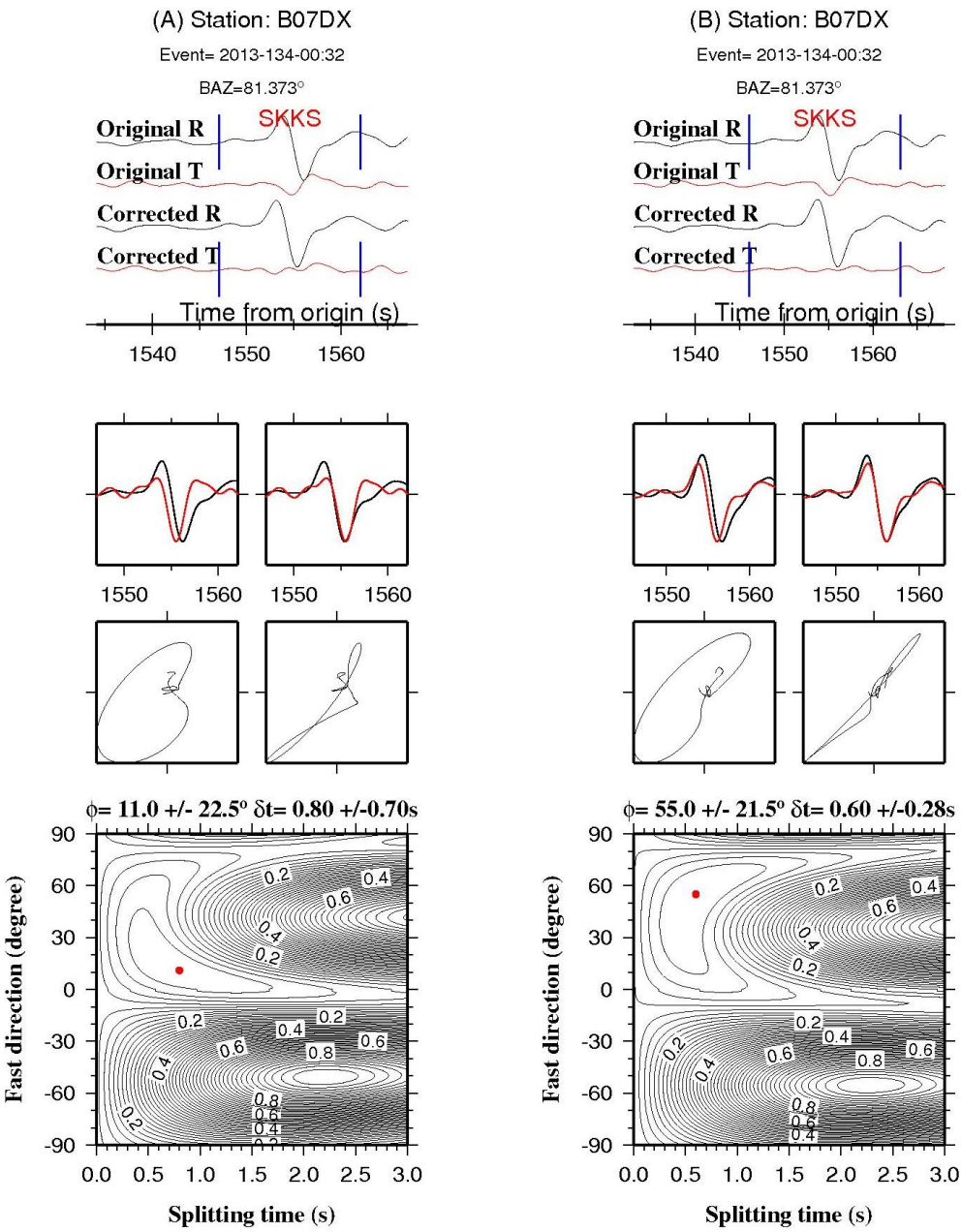

Figure 3. An SKKS measurement from station B07DX (at which the N-S component has an orientation of -11°) calculated using (A) the original and (B) station-orientation corrected dataset, respectively. (Top) Original and corrected XKS radial and transverse component seismograms. (Middle) Pre- and post-correction fast and slow waveforms and particle motion patterns. (Bottom) Contour maps of transverse component energy. The red dot on the contour map indicates the optimal splitting parameters.

3.2 Spatial distribution of XKS splitting parameters

A total of 223 pairs of Quality A or B splitting parameters were obtained at the 22 stations, including 73 PKS, 58 SKKS, and 92 SKS measurements from a total of 91 teleseismic events (Fig. 2c). Examples for each of the three XKS phases are demonstrated in Fig. 4. No systematic azimuthal variations of the splitting parameters are observed (Fig. 5), suggesting that a single layer of anisotropy with a horizontal axis of symmetry is sufficient to explain the observed SWS parameters (Silver and Savage, 1994). The fast orientations are dominantly NE-SW with an average value of 37.5±20.6° (Figs. 1 and 2, Table 2), which is consistent with the APM direction of the African plate in the study area based on the NUVEL-1A model (DeMets et al., 1994). The mean splitting time is 1.09±0.34 s and is comparable with the global average of 1.0 s for continents (Silver, 1996), but is larger than the 0.62±0.02 s observed at the 59 non-null SASE stations (Silver et al., 2001). Under the assumption of a 4% anisotropy (Mainprice et al., 2000), the thickness of the anisotropy layer that produces the observed anisotropy is about 120 km on average.

Based on the location of the tectonic boundaries (Begg et al., 2009; McCourt et al., 2013) and the characteristics of the observed splitting parameters, we divide the measurements into 4 groups (Fig. 2a). The 8 measurements in Area A (Figs. 5a and 5b) have the surface projection of their ray-piercing points (calculated at the depth of 200 km) on the Congo craton. The mean splitting parameters are 51.4±26.1° for θ, and 1.05±0.30 s for δt. The 47 Area B measurements are in the ORZ, with corresponding mean splitting parameters of 30.5±19.4° and 1.13±0.30 s (Figs. 5c and 5d). Area C includes 86 measurements in the Magondi belt and the southern half of the Rehoboth Province (Figs.

5e and 5f). The mean splitting parameters are 27.5±17.4° and 1.12±0.39 s. The most significant spatial variation of the splitting parameters in the entire study is found near the SE end of Area C (Fig. 2a). Area D belongs to the Kalahari craton (mostly the Limpopo belt). It has 82 measurements (Figs. 5g and 5h) and the mean splitting parameters are 50.78±15.3° and 1.03±0.41 s.

Table 2. Station-averaged splitting parameters

Station			θ			δt			No.
Name	Lat.	Lon.							
	deg.	deg.		deg.			s		events
B01KR	-22.238	26.718	42	±	14	1.13	±	0.4	15
B02LT	-21.393	25.581	52	±	11	1.06	±	0.2	19
B03SL	-21.121	24.764	22	±	14	1.04	±	0.3	21
B04KH	-20.474	24.514	20	±	10	1.31	±	0.5	31
B05MO	-20.218	24.132	22	±	14	0.87	±	0.3	16
B06OR	-19.901	23.527	37	±	14	1.19	±	0.3	15
B07DX	-20.549	22.749	55	±	14	1.09	±	0.3	8
B08TS	-20.164	22.459	57	±	13	1.34	±	0.3	7
B09NK	-19.663	22.194	30	±	9	1.15	±	0.3	3
B10PP	-18.913	22.543	24	±	12	1.19	±	0.4	11
B11ET	-19.016	22.316	17	±	15	0.94	±	0.2	4
B12SS	-18.746	22.197	78	±	8	0.99	±	0.4	4
B13NX	-18.579	21.994	44	±	18	1	±	0.6	3
B14MH	-18.295	21.792	15	±	15	0.65	±	0.2	1
B15MW	-19.631	23.827	26	±	15	1.11	±	0.2	11
B1665	-22.825	27.229	51	±	22	0.73	±	0.3	7
B17CI	-19.294	22.909	22	±	13	0.9	±	0.2	6
SA64	-22.969	26.202	56	±	17	0.85	±	0.4	3
SA65	-22.818	27.222	45	±	15	1.02	±	0.3	5
SA66	-21.900	26.373	61	±	12	1.09	±	0.2	10
SA67	-21.886	27.274	59	±	7	0.99	±	0.2	6
SA70	-21.088	26.335	48	±	13	1.13	±	0.3	17

3.3 Relationship with SWS studies from adjacent areas

All of the previous studies in adjacent areas reported their results in the form of station-averaged parameters, which are largely consistent with those obtained at 22 stations measured by this study (Fig. 1). Barruol and Ismail (2001) used African IRIS and Geoscope permanent stations to investigate upper mantle anisotropy, including station TSUM in Namibia near the southern border of the Congo craton as well as station LSZ in Zambia northeast of the ORZ (Fig. 1). Both LSZ and TSUM display SWS parameters consistent with our findings, i.e., a nearly NE-SW fast orientation (16° and 31°, respectively) and small splitting time (0.73 s and 0.43 s, respectively) without evidence of azimuthal variations. Similarly, relatively small splitting times are observed for the SAFARI stations near the Congo craton (e.g., B14MH and B13NX) while relatively larger splitting times are reported for stations within the ORZ (about 1.13 s on average).

Among the 17 SAFARI stations, three (B01KR, B02LT, and B1665) are within the study area of the SASE project (Silver et al., 2001). The resulting SWS parameters from the three SAFARI stations are remarkably consistent with those from the five SASE stations along the profile (Silver et al., 2001). The average fast orientation and splitting time of the five SASE stations are 53.4±14.6° and 1.07±0.25 s, while those of the three SAFARI stations are 48.2±15.7° and 1.03±0.35 s. The individual SWS measurements demonstrating an approximate E-W fast orientation are similar with the station-averaged SWS measurements obtained by Silver et al. (2001) from other SASE stations within the Limpopo belt (Figs. 1 and 2).

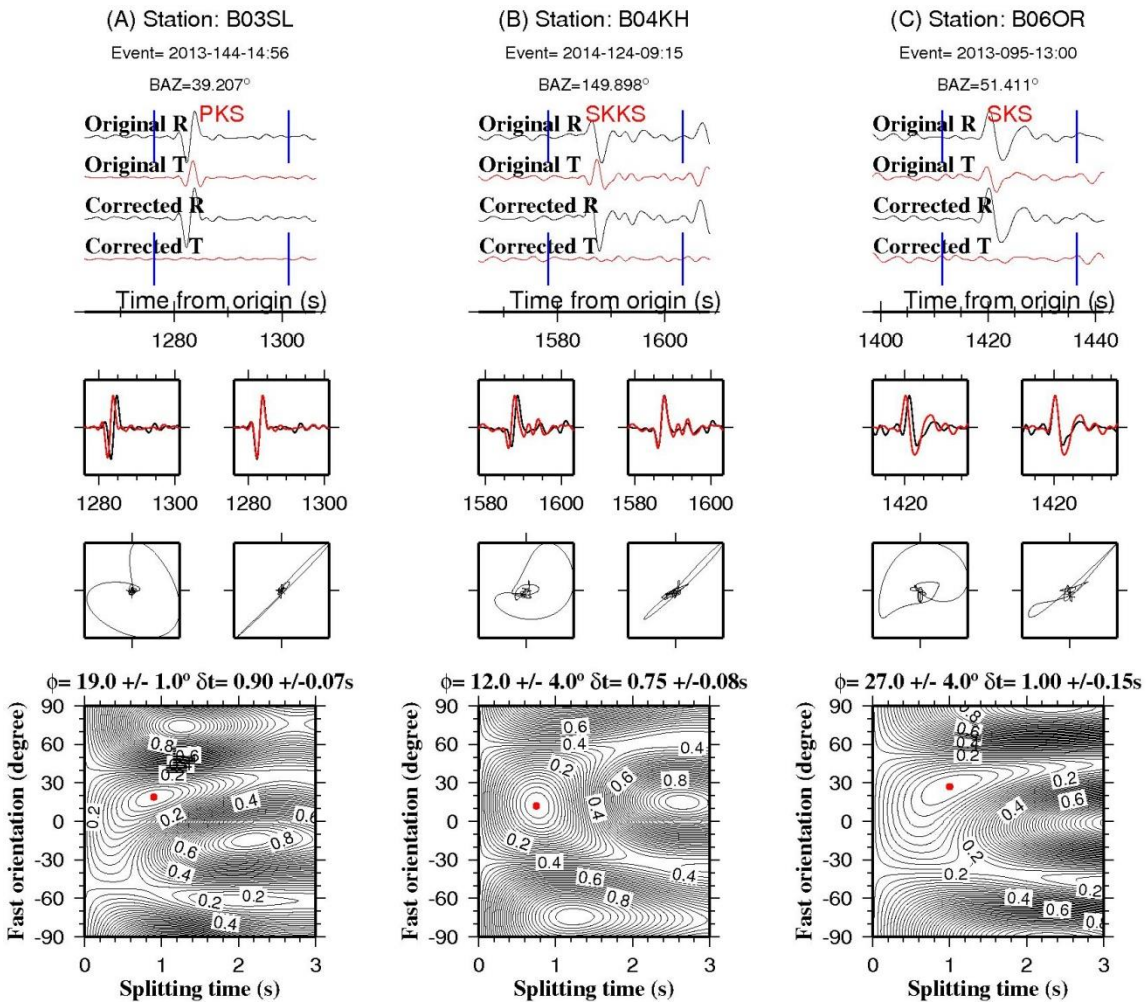

Figure 4. Same as Fig. 3 but for examples of each of the XKS phases (PKS, SKKS and SKS) used in the study recorded by 3 different stations. The waveforms have been corrected for station mis-orientation.

4. Discussion

4.1 Estimating the depth of anisotropy

The epicentral distance of the SKS, SKKS, and PKS arrivals used in the study is equal to or greater than 84°, 95°, and 120°, respectively. For SKS, this corresponds to a ray parameter of 6.532 s/degree or smaller, and an angle of incidence of smaller than 16° at 200 km depth measured from the vertical. Similarly, the maximum angle of incidence

at 200 km depth for the SKKS and PKS phases is about 18° and 5°, respectively. Therefore, the XKS phases arrive at a steep angle of incidence and thus have an excellent lateral but poor vertical resolution, resulting in uncertainties and debates in the tectonic interpretations of the observed SWS measurements.

A technique commonly employed to estimate anisotropy depth is the intersecting Fresnel-zone approach (Alsina and Snieder, 1995) which is based on the analysis of the size for the first Fresnel zones of close-proximity XKS raypaths. However, such a technique is limited to the case wherein significant lateral variations in seismic anisotropy exist between nearby stations, or when a station samples two regions with different splitting parameters (see Lemnifi et al., 2015 for an example in Libya).

In this study, we apply a more generalized and quantitative extension of the intersecting Fresnel zone approach based on the spatial coherency of splitting parameters (Liu and Gao, 2011). This technique employs the idea that the observed splitting parameters will reach the highest spatial coherency if the assumed anisotropy depth is correct. Several conditions must be satisfied prior to applying this technique, the first of which is the compilation of a high-quality data set of individual (rather than station-averaged) splitting parameters, and the other is that there must exist a significant but smooth spatial variation in the splitting parameters which should simultaneously signify a single layer of anisotropy (Liu and Gao, 2011). We find that the observed SWS measurements in Area C possess significant spatial variations (Fig. 2a) and satisfy the other conditions mentioned above, and can be used to estimate the depth of anisotropy.

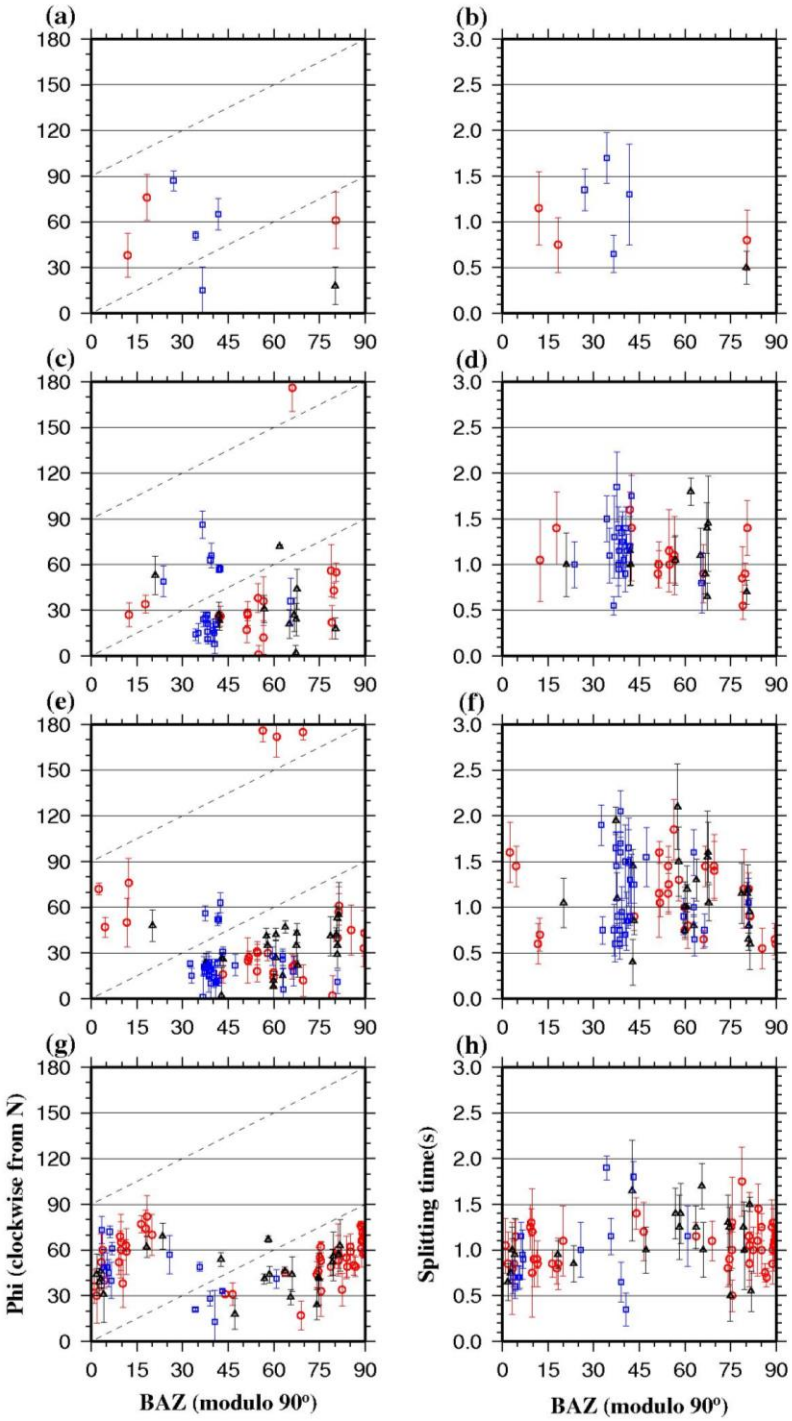

Figure 5. Azimuthal variations of resulting fast orientations (left panels) and splitting times (right panels) for (a, b) Area A, (c, d) Area B, (e, f) Area C, and (g, h) Area D measurements. Blue squares, black triangles and red circles represent PKS, SKKS, and SKS phases, respectively. The dashed lines show the situation when the BAZ equals θ or θ+90°, i.e., along the lines null measurements are expected (and this is why there are no well-defined measurements along the lines).

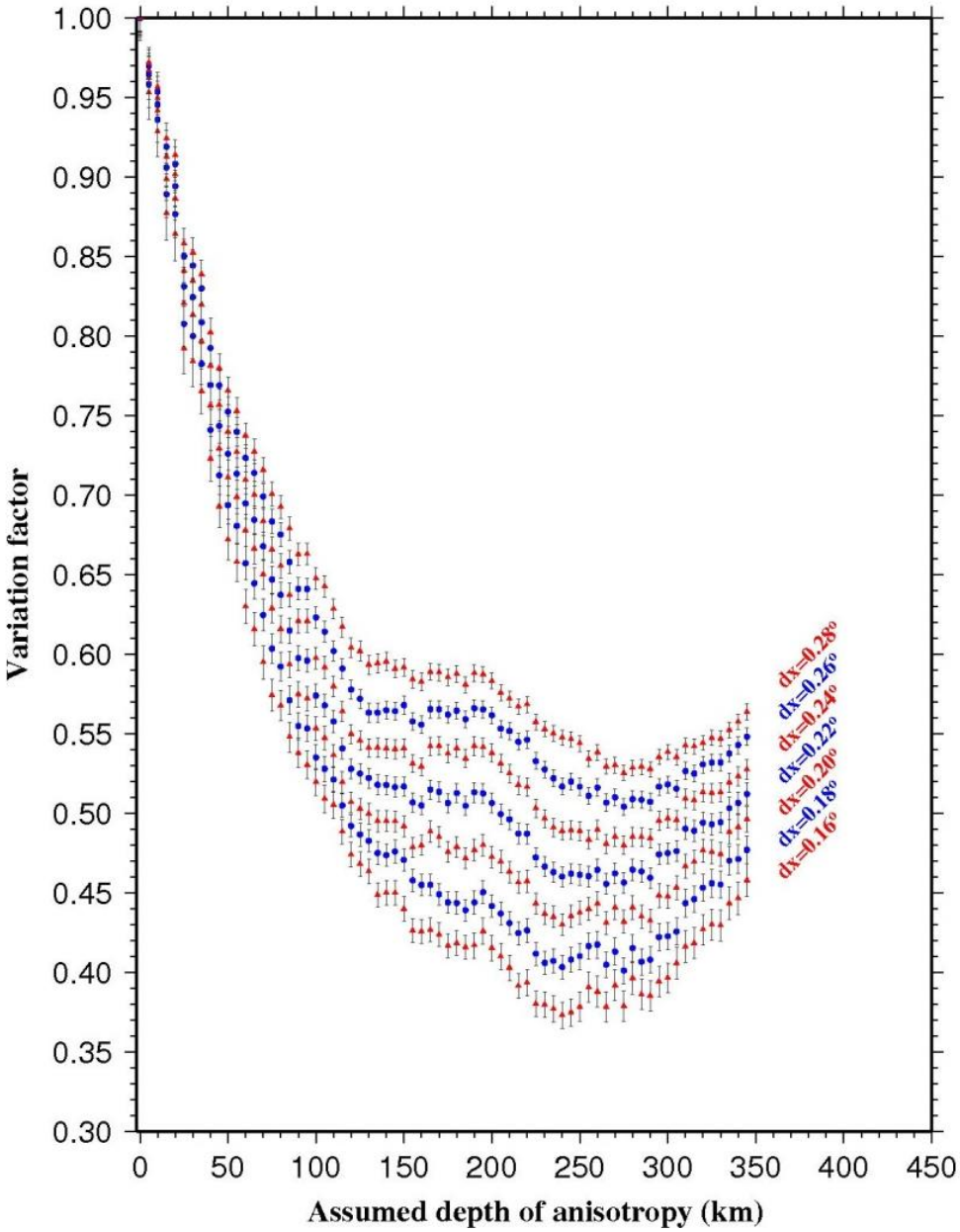

Figure 6. Anisotropy analysis for the SWS measurements in Area C based on the spatial coherence technique (Liu and Gao, 2011), resulting in an optimal depth of anisotropy between 240-280 km.

The optimal anisotropy depth is searched in the range of 0 to 350 km at an interval of 5 km. It corresponds to the minimum spatial variation factor (Fv), which is defined in Eqs. 4-7 in Liu and Gao (2011). The block size (dx) used to calculate the Fv

should be given a proper value due to the fact that smaller dx will bring unstable Fv depth variations and uncertainties, while larger dx leads to a broadened Fv curve and reduces the peak-to-peak amplitude (Liu and Gao, 2011). In this study, experimental values of dx from 0.16° to 0.28° with an interval of 0.02° have been employed to generate the Fv curves (Fig. 6).

The resulting Fv curves suggest that the optimal depth of the center of the anisotropic layer is between about 240 to 280 km, which is similar to the lithospheric thickness based on the tomography results for southern Africa (James et al., 2001). Beneath the vicinity of the ORZ, magnetotelluric studies suggested a lithospheric thickness of about 180 km (Miensopust et al., 2011). Thus it can be safely concluded that the anisotropy originates primarily from the upper asthenosphere beneath the ORZ, which is similar to the conclusion proposed by Vinnik et al. (1996) for the Kaapvaal craton. It must be mentioned, however, that due to a lack of spatial variations of the splitting parameters in Areas A, B, and D, the depth of the source of the observed anisotropy cannot be estimated beneath these areas; however, as discussed below, although lithospheric contributions cannot be completely ruled out, the observations can best be explained if they have an asthenospheric origin.

4.2 Constraints on rifting mechanisms

The similarity between the APM direction and the trend of most of the tectonic boundaries in the study area makes it difficult to distinguish a lithospheric origin from an asthenospheric one. In addition to the results of depth estimation, which favors an upper asthenospheric origin, another piece of evidence arguing against a dominantly

lithospheric origin can be found along the boundary between the Zimbabwe craton and the Limpopo belt (Fig. 2), where all the fast orientations are almost orthogonal (rather than parallel, as expected for a lithospheric origin) to this major tectonic boundary. Additionally, the ORZ, which is characterized by a relatively thin lithosphere compared to the adjacent cratonic terranes based upon magnetotelluric and tomographic studies (James et al., 2001; Miensopust et al., 2011), exhibits slightly larger splitting times than the Kalahari craton. One would expect to observe smaller splitting times in regions with thin lithosphere if the anisotropy is the result of uniform strain pervading the continental lithosphere (Silver and Chan, 1991). This interpretation is also consistent with the fact that the SASE stations (Silver et al., 2001), most of which overly the thicker lithosphere of the Kalahari craton, show smaller splitting times with a mean value of 0.62±0.02 s (and about 1/4 of the stations show no splitting) relative to the SAFARI stations (1.09±0.34 s).

In the following, we examine a number of possible geodynamic models for the initiation and development of continental rifting, under the assumption that the observed anisotropy primarily reflects simple shear in an approximately 120 km thick layer in the upper-most asthenosphere.

4.2.1 Active rifting

Active rifting models (e.g., Sengor and Burke, 1978) advocate the dominant role of mantle flow, presumably associated with a mantle plume, on continental breakup. For a stationary lithosphere relative to the asthenosphere, the horizontal component of the

flow system is expected to have a pattern that is radiating away from the center of the plume, and for a moving lithosphere, a parabolic pattern is predicted (Karato et al., 2008).

The existence of such a plume beneath the ORZ is possible, due to the fact that the ORZ is developing directly above the proposed African superplume (Ritsema et al., 1998). The expected radiating or parabolic pattern of the fast orientations, however, is not observed beneath the ORZ or in southern Africa (Fig. 1), leading to doubts about the existence of an active mantle plume beneath the area. Such a conclusion is consistent with the observations of normal mantle transition zone thickness using the same dataset (Yu et al., in review).

4.2.2 Edge-driven mantle convection

The thin lithosphere beneath the ORZ relative to the Congo craton could induce a small-scale mantle convection system due to lateral temperature variations (King and Anderson, 1998). This mechanism has been used to explain the formation of zones of continental extension such as the Cameroon volcanic line (Koch et al., 2012). If this process contributes significantly to the observed anisotropy, the fast orientations in the vicinity of the ORZ should be mostly orthogonal to the trend of the rift. We observed dominantly rift-parallel fast orientations and thus conclude that edge-driven small-scale convection is not the source of the observed anisotropy.

4.2.3 Rifting induced by intra-plate relative motion

The ORZ is developing primarily within the Damara orogenic belt between the Archean Congo and Kalahari cratons. The consistently NE-SW fast orientations are

largely in agreement with those observed in surrounding areas. Though the African plate has a general northeastward motion based on the NUVEL-1A model (DeMets et al., 1994), it has been suggested that South Africa is currently rotating clockwise relative to the Nubian plate, probably along the Damara belt (Malservisi et al., 2013).

Numerical modeling shows that topography of the lithosphere-asthenosphere boundary exerts a strong control on the direction and magnitude of stress transfer from the asthenosphere to the lithosphere (O'Neill et al., 2010). In addition, increased plate-mantle coupling beneath thick continental lithosphere may increase plate-driving forces, surface deformation, and mantle-derived lithospheric stresses in these regions (Conrad and Lithgow-Bertelloni, 2006). Therefore, contrasts in lithospheric thickness between the Congo craton, the ancient orogenic belts, and the Kalahari craton can possibly lead to differential basal drag forces beneath different areas, leading to spatially-varying plate motion velocities. The relative movements between the Archean cratons could rupture ancient zones of lithospheric weakness such as the Damara belt and exert a trans-tensional force upon the lithosphere, resulting in the initiation of continental rifting.

This model suggests a passive role of mantle flow in the initiation and development of the ORZ. Given the consistency between the APM and the fast orientations revealed by this and previous studies (Fig. 1), we propose that simple shear in the direction of the APM developed in the upper asthenosphere contributes the bulk of the observed anisotropy. Deviations of the fast orientation observed in Area C can be explained as the modulation of flow by the topography of the bottom of the lithosphere, as proposed for North America (Fouch et al., 2000; Refayee et al., 2014) and northern Africa (Miller et al., 2013; Lemnifi et al., 2015). The model is consistent with surface

wave studies which demonstrate the existence of asthenospheric plate-parallel polarization of azimuthal anisotropy beneath southern Africa (Adam and Lebedev, 2012), and with findings from a joint inversion of P-wave receiver functions and SWS waveforms (Vinnik et al., 2012).

Finally, this study provides additional constraints on the APM direction of the African plate. Mostly due to the fact that Africa is a slow-moving plate, the APM direction varies dramatically among different models (e.g., DeMets et al., 1994; Gripp and Gordon, 2002; Kreemer, 2009; Altamimi et al., 2011). The consistently NE-SW fast orientations across the study area and most of southern Africa place more weight on models with a NE APM direction for southern Africa.

5. Conclusion

In this study, we employed recently archived broadband seismic data in the vicinity of the ORZ to conduct the first SWS investigation of the incipient rift. The resulting mantle anisotropy shows a dominantly NE-SW orientation which is parallel to the African APM. Although significant contributions from the lithosphere to the observed anisotropy cannot be completely ruled out, spatial coherency analysis of the splitting parameters and correspondence with geological features suggest that the center of the approximately 120 km thick anisotropic layer is located between the depth of 240 and 280 km, implying an asthenospheric origin of anisotropy, probably as the result of simple shear in the boundary layer between the lithosphere and the asthenosphere. Comparison of the resulting SWS measurements with predicted mantle flow directions originating from an active mantle plume or edge-driven small-scale mantle convection suggests that

neither is operating beneath the incipient rift. The measurements advocate a new model of continental rifting, in which differential basal drag applied to cratonic blocks results in relative intra-plate movements and leads to rifting along ancient orogenic zones, which are areas of mechanical weakness.

III. DETERMINING CRUSTAL STRUCTURE BENEATH SEISMIC STATIONS OVERLYING A LOW-VELOCITY SEDIMENTARY LAYER USING RECEIVER FUNCTIONS

Abstract

The receiver function (RF) technique has been widely applied to investigate crustal and mantle layered structures using P-to-S converted (Ps) phases from velocity discontinuities. However, the presence of low-velocity (relative to that of the bedrock) sediments can give rise to strong reverberations in the resulting RFs, frequently masking the Ps phases from crustal and mantle boundaries. Such reverberations are caused by P-to-S conversions and their multiples associated with the strong impedance contrast across the bottom of the low-velocity sedimentary layer. Here, we propose and test an approach to effectively remove the near surface reverberations and decipher the Ps phases associated with the Moho discontinuity. Auto-correlation is first applied on the observed RFs to determine the strength and two-way travel-time of the reverberations, which are then used to construct a resonance-removal filter in the frequency domain to remove or significantly reduce the reverberations. The filtered RFs are time-corrected to eliminate the delay effects of the sedimentary layer and applied to estimate the sub-sediment crustal thickness and Vp/Vs using a H-k stacking procedure. The resulting sub-sediment crustal parameters (thickness and Vp/Vs) are subsequently used to determine the thickness and Vp/Vs of the sedimentary layer, using a revised version of the H-k stacking procedure. Testing using both synthetic and real data suggests that this computationally inexpensive technique is efficient in resolving sub-sediment crustal properties beneath stations sitting

on a low-velocity sedimentary layer, and can also satisfactorily determine the thickness and Vp/Vs of the sedimentary layer.

1. Introduction

P-to-S converted phases and their multiples (hereafter collectively called the Ps phases) related to the Moho including PmS, PPmS, and PSmS (Figure 1) have been widely employed to image crustal thickness and Vp/Vs beneath a recording site using the receiver function (RF) technique (Langston, 1979; Owens et al., 1984; Ammon, 1991; Zandt and Ammon, 1995; Zhu and Kanamori, 2000). However, the existence of a low-velocity sedimentary layer poses significant problems to successfully apply the RF technique (Zelt and Ellis, 1999). The large acoustic impedance (product of velocity and density) contrast between the low-velocity sedimentary layer and the crystalline crust can give rise to strong P-to-S wave conversions and near surface reverberations, significantly masking the Ps phases associated with the Moho (Langston, 2011). Consequently, the conventional H-k (crustal thickness-Vp/Vs) stacking technique (Zhu and Kanamori, 2000) usually leads to erroneous results. Yeck et al. (2013) estimated that a deep basin could contribute to an error of more than 10 km in the resulting crustal thickness if the sedimentary effects are not correctly accounted for.

A variety of teleseismic techniques have been proposed and developed for the purpose of determining both the sedimentary and crustal structures. Forward modeling was conducted to obtain sedimentary and crustal S-wave velocity models by iteratively fitting the synthetics to the observed RFs (Sheehan et al., 1995; Zelt and Ellis, 1999; Clitheroe et al., 2000; Anandakrishnan and Winberry, 2004; Mandal, 2006; He et al.,

2012), but the strong near surface reverberations on the resulting radial RFs make it difficult to reliably determine the best fitting synthetics (Clitheroe et al., 2000). Langston (2011) used the bed-rock structure of stations close to the sedimentary area as priori crustal parameters to isolate the up-going S-wave field from the total teleseismic response of the P-wave for stations within the sedimentary basin, using the theory of wave-field continuation and decomposition (Thorwart and Dahm, 2005; Bostock and Trehu, 2012). Recently, Tao et al. (2014) improved the technique of Langston (2011) by minimizing the up-going S-wave energy without the need for the reference stations. The computationally intensive approach of wave-field continuation and decomposition is effective in obtaining reliable crustal parameters beneath sedimentary basins, under the condition when the densities and P-wave velocities of the involved layers (sediment, crust and mantle) are known. Yeck et al. (2013) proposed a sequential two-layer H-k stacking method to determine the sedimentary and crustal structures. This technique works the best when the Moho Ps phases are not entirely masked by the sedimentary reverberations (Yeck et al., 2013). In addition, some recent studies attempted to reduce the influence of the sedimentary layer by applying band-pass or band-rejection filters (Leahy et al., 2012; Reed et al., 2014), but it is sometimes subjective to decide the optimal frequency bands and the removal of the sedimentary effects is frequently incomplete.

Although reverberations associated with a low-velocity sedimentary layer can partially or totally mask the Moho Ps phases, as described below, we find that they can be effectively removed or significantly reduced by applying a resonance-removal filter. The parameters needed to construct the filter are taken directly from the observed RFs. The filtered RFs are then utilized to obtain sub-sediment crustal thickness and Vp/Vs, and are

subsequently used to obtain the thickness and Vp/Vs of the sedimentary layer. Similarly to the standard H-k stacking technique (Zhu and Kanamori, 2000), the approach requires P-wave velocities but not the densities of the involved layers.

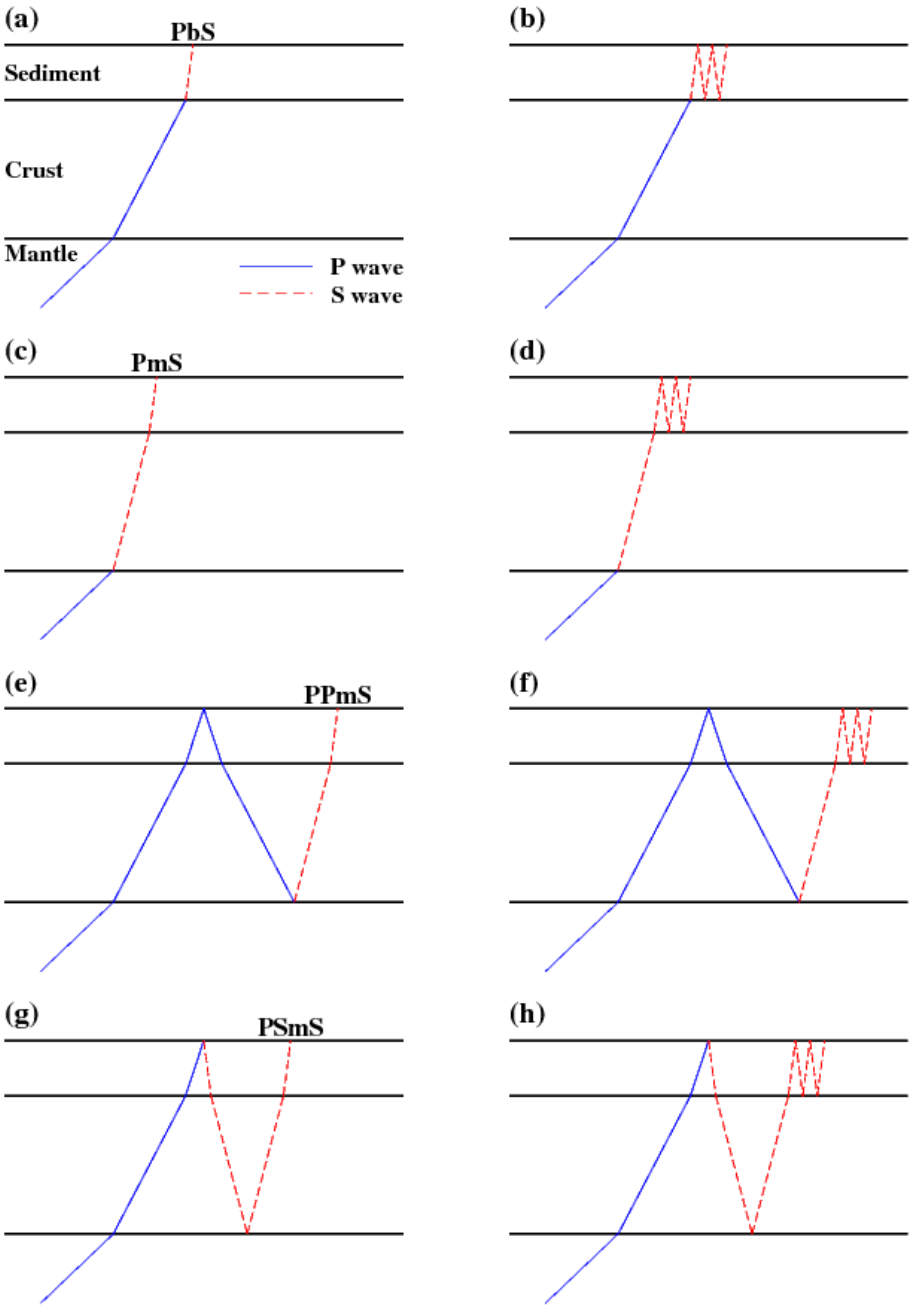

Figure 1. Schematic diagrams showing the main Ps phases (left columns) and their reverberations in the sedimentary layer (right columns).

2. Methods

2.1 Receiver Function

Teleseismic waves travel through the interior of the Earth and are recorded by seismic stations at the surface. The conversion from compressional to shear waves occurs when P-waves encounter an acoustic impedance interface within the Earth. The recorded seismic waveforms are the combined results of the source time function, travel path, and local structure (Burdick and Langston, 1977; Langston, 1979). Due to the steep angle of incidence of teleseismic waves near the surface, most of the shear wave energy is recorded in the radial component while the vertical component is predominantly occupied by the compressional wave. The Ps phases can be source-normalized by deconvolving the vertical component from the corresponding section of the radial component (Ammon, 1991). The resulting time series reflect the relative responses of the Earth structure near the receiver and are named as receiver functions (Langston, 1979). The receiver functions used in the study were generated by employing the water-level deconvolution technique (Ammon, 1991), which is a division in the frequency domain, with a water-level of 0.05 and a Gaussian width factor of 5.0.

The Ps phases in the resulting RFs can be expressed as (Ammon, 1991)

$$F(t) = A_s \delta(t - t_s) \tag{1}$$

Where $\delta(t - t_s)$ is a Dirac delta function, and A_s and t_s represent the corresponding amplitudes and time delays, respectively, of the P s phases (including direct conversions such as PmS and multiples such as PPmS and PSmS, see Figure 1). The reference time ($t = 0$) corresponds to the arrival time of the direct P−wave. A

popularly used procedure for crustal studies using RFs is H−k stacking, in which the radial RFs are moveout-corrected and stacked along the travel time curves of the Moho Ps phases at each candidate pair of H (thickness) and k (Vp/Vs) in a grid-search procedure (Chevrot and Van der Hilst, 2000; Zhu and Kanamori, 2000; Nair et al., 2006; Bashir et al., 2011). The maximum stacking amplitude corresponds to the optimal crustal thickness and Vp/Vs.

2.2 Effects of a Low-velocity Sedimentary Layer

It has long been recognized that a low-velocity sedimentary layer of a few km or thinner (Figure 1) can result in prominent high-amplitude, low-frequency reverberations. Relative to RFs recorded by stations on bedrock, the width of the first P arrival is broadened and its amplitude is decreased (Zelt and Ellis, 1999). On the RFs, the amplitude of the first Ps phase from the bottom of the sedimentary layer (hereafter named PbS phase, with one S−wave leg in the sedimentary layer, see Figure 1a) can become so high that the direct P-wave is usually completely masked. Such RFs are characterized by a delayed first peak corresponding to the arrival of the PbS (Yeck et al., 2013) (Figure 2a).

The large impedance contrasts across the bottom of the sedimentary layer and that from the free surface create strong reverberations in the form of multiples. Similar to multiples created in a water-layer (e.g., Equation 18 in Stoffa et al., 1974), for a model with a low-velocity sedimentary layer (Figure 1), the primary and multiples of the converted shear-waves (Figure 1) can be expressed as

$$H(t) = \sum_{n=0}^{\infty}(-r_0)^n \times F(t - n \times \Delta t) \quad (2)$$

Where n is the index of the nth reverberation of the converted shear phases, r_0 is the strength (proportional to the reflection coefficient at the bottom of the sedimentary layer) of the near surface reverberations, Δt is the two-way travel-time for the reverberations of the converted waves in the sedimentary layer, and $F(t)$ is the RF without the influence of the sedimentary layer (Equation 1). Note that for $n = 0$, $H(t)$ equals $F(t)$ and represents the primary arrivals; and for $n = 1$ (the first reverberation), the arrivals have a negative polarity (due to the reflection from the free surface) and a delay time of Δt relative to the direct phase. Due to the steep incident angle of PbS and the large acoustic impedance contrast across the bottom of the sedimentary layer, the dominant energy in the RFs is the reverberations of PbS, followed by those of PmS, PPmS, and PSmS in the sedimentary layer (Figure 1). Synthetic tests show that PPbS and PSbS and their reverberations are much weaker than the corresponding PbS phases, mostly because of the near-vertical raypaths associated with the small sedimentary velocities, and the consequent inefficiency in producing converted S-waves.

In the frequency domain, Equation 2 can be expressed as

$$H(i\omega) = F(i\omega) \sum_{n=0}^{\infty} (-r_0)^n \times e^{-i\omega n \Delta t}, \quad (3)$$

Where i is the complex symbol, and $\sum_{n=0}^{\infty} (-r_0)^n \times e^{-i\omega n \Delta t}$ is a geometric series that can be simplified as $(1 + r_0 e^{-i\omega \Delta t})^{-1}$. Thus $F(t)$ can be obtained in the frequency domain using

$$F(i\omega) = H(i\omega)\left(1 + r_0 e^{-i\omega \Delta t}\right), \quad (4)$$

$F(i\omega)$ is the RF in the frequency domain after the removal of the sedimentary reverberations. Using the above equation, near surface reverberations can be eliminated

from the observed RF spectrum ($H(i\omega)$) by designing a resonance-removal filter of the form ($1 + r_0 e^{-i\omega\Delta t}$). An example of such a filter in both the frequency and time domains is shown in Figure 2. Such a filter has been widely applied in petroleum exploration to quantify and remove multiples especially those associated with a surface water layer (Stoffa et al., 1974; Yilmaz, 2001).

The strength of the reverberations (r_0) required by the filter can be directly measured from the original RFs (Figure 2a) as the ratio between the amplitude of the first trough and that of the first peak, and the two-way travel-time (Δt) can be measured using the time separation between the first peak and first trough. However, as routinely used in exploration seismology (e.g. Yilmaz, 2001), they can be more reliably determined from the normalized auto-correlation function (Figure 2b), which has a unity amplitude (and thus the ratio is equivalent to the amplitude of the first trough on the auto-correlation function) and is centered at $t = 0$ (and thus the time separation is the same as the time of the first trough). Due to varying angle of incidence of different RFs, in reality these two parameters are calculated for each of the RFs. Obviously, this procedure is applicable for reverberations with a single dominant frequency. After the removal of the reverberations, PbS and the Moho Ps phases show up clearly in the filtered RFs (Figure 2e). The direct P phase, which arrives at $t = 0$, is weaker than PbS and can barely be seen unless the frequency of the wavelet is unrealistically high.

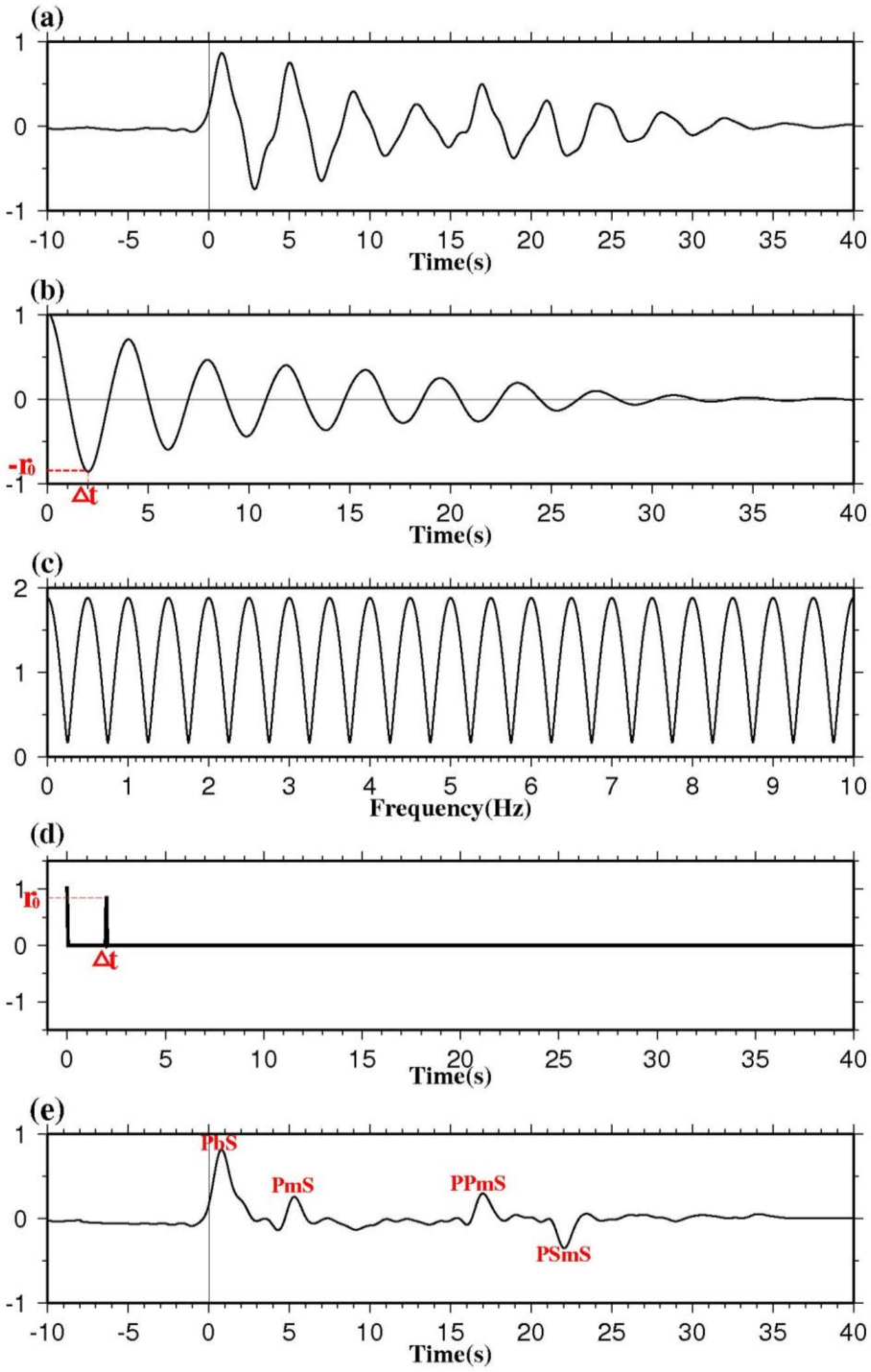

Figure 2. (a) Synthetic RF. Note that the first peak is delayed by about 1 s and represents the P-to-S converted phase from the bottom of the sedimentary layer. (b) Auto-correlation of the RF shown in (a). Δt and r_0 are the two-way travel-time and strength of the sedimentary reverberations, respectively. (c) Frequency domain plot of a resonance-removal filter with r_0=0.8 and Δt=2.0 s. (d) Same as (c) but in the time domain. (e) Resulting RF after applying the resonance-removal filter.

2.3 Determination of Sub-sediment Crustal Thickness and Vp/Vs

The H-k stacking method (Zhu and Kanamori, 2000) can then be employed to estimate crustal thickness and Vp/Vs using the filtered RFs. However, due to the delay effects of the sedimentary layer, the conventional H-k stacking technique would result in a larger than real crustal thickness if time delays associated with the sedimentary layer are not corrected (Yeck et al., 2013). Here we use the arrival time of the PbS phase and the two way travel-time of the reverberations to time-correct the filtered RFs. The sub-sediment crustal thickness and Vp/Vs can be obtained by applying a time-corrected H− k stacking formula of the form

$$A(H_i, k_j) = \sum_{m=1}^{N} \omega_1 \times S_m\left(t_1^{(i,j)} + \delta t_m\right) + \omega_2 \times S_m\left(t_2^{(i,j)} + \Delta t_m - \delta t_m\right) - \omega_3 \times S_m\left(t_3^{(i,j)} + \Delta t_m\right) \quad (5)$$

Where i and j are indexes for the candidate sub-sediment crustal thickness (H_i) and Vp/Vs (k_j) respectively; $A(H_i, k_j)$ is the stacking amplitude corresponding to the candidate pair of H_i and k_j; N is the number of RFs participated in the stacking; $S_m(t)$ is the amplitude of the point on the mth RF at time t after the direct P-wave; ω_1, ω_2 and ω_3 are weighting factors that satisfy $\omega_1 + \omega_2 + \omega_3 = 1$ (Zhu and Kanamori, 2000) for PmS, PPmS, and PSmS (Figure 1), respectively; δt_m is the time delay (relative to the direct P-wave) of the PbS phase on the m th RF; Δt_m is the two-way travel-time of the reverberations obtained from auto-correlation of the mth RF; and $t_1^{(i,j)}$, $t_2^{(i,j)}$ and $t_3^{(i,j)}$ correspond to the theoretical moveout of PmS, PPmS and PSmS phases in the sub-

sediment crust. The optimal pair of H_i and k_j corresponds to the maximum amplitude of $A(H_i, k_j)$.

To better understand the time terms in Equation (5), let us consider a hypothetical situation of vertical incidence, for which the delay time of the PbS phase, $\delta t = \frac{H_d}{V_s} - \frac{H_d}{V_p}$, and the reverberation period or two-way travel-time of PbS, $\Delta t = 2\frac{H_d}{V_s}$, where H_d is the thickness of the sedimentary layer. The PmS phase travels through the sedimentary layer once as an S−wave (Figure 1c) and thus the S− and P−wave differential time after traveling through the sedimentary layer is $\frac{H_d}{V_s} - \frac{H_d}{V_p}$ which is δt. The PPmS phase, on the other hand, has two P− legs and an S− leg in the sedimentary layer, and thus the S− and P−wave differential travel time is $\frac{H_d}{V_s} + 2\frac{H_d}{V_p} - \frac{H_d}{V_p}$ which happens to be $\Delta t - \delta t$. Finally, the PSmS phase has two S−legs and one P− leg in the sedimentary layer, and thus the differential time is Δt. After the removal of the travel-times associated with the low-velocity sedimentary layer, the station is virtually downward projected to the bottom of the sedimentary layer. Consequently, the optimal thickness and Vp/Vs of the sub-sediment crust are determined.

2.4 Determination of Sedimentary Thickness and Vp/Vs

We next propose a procedure to grid-search for the optimal thickness and Vp/Vs of the sedimentary layer using the resulting sub-sediment crustal thickness and Vp/Vs. The phases that we use for this task are PbS, PPmS, and PSmS (note that the last two are not PPbS and PSbS which are too weak to be used, as discussed above). At first glance, it seems that PPmS and PSmS are associated with the Moho and not the sedimentary layer.

However, because they travel through both the sub-sediment crustal and the sedimentary layers, their arrival times are functions of the thickness and Vp/Vs of both layers, as quantified in Equations 7-9.

The grid-search is conducted using

$$A(H_i, k_j) = \sum_{m=1}^{n} \omega_4 \times S_m\left(t_4^{(i,j)}\right) + \omega_2 \times S_m\left(t_2^{(i,j)}\right) - \omega_3 \times S_m\left(t_3^{(i,j)}\right) \quad (6)$$

Where H_i and k_j indicate a pair of candidate sedimentary thickness and Vp/Vs; ω_4, ω_2 and ω_3 are the weighting factors for PbS, PPmS and PSmS, respectively; and $t_4^{(i,j)}$, $t_2^{(i,j)}$ and $t_3^{(i,j)}$ are the moveout of PbS, PPmS and PSmS phases through the sedimentary and sub-sediment crustal layers calculated using the following equations

$$t_4^{(i,j)} = \int_{-H_i}^{0}\left(\sqrt{\left(\frac{V_p(z)}{k_j}\right)^{-2} - p^2} - \sqrt{\left(V_p(z)\right)^{-2} - p^2}\right)dz \quad (7)$$

$$t_2^{(i,j)} = \int_{-H_i}^{0}\left(\sqrt{\left(\frac{V_p(z)}{k_j}\right)^{-2} - p^2} + \sqrt{\left(V_p(z)\right)^{-2} - p^2}\right)dz + \int_{-(H_i+H_c)}^{-H_i}\left(\sqrt{\left(\frac{V_p(z)}{k_c}\right)^{-2} - p^2} + \sqrt{\left(V_p(z)\right)^{-2} - p^2}\right)dz \quad (8)$$

$$t_2^{(i,j)} = \int_{-H_i}^{0} 2\sqrt{\left(\frac{V_p(z)}{k_j}\right)^{-2} - p^2}\,dz + \int_{-(H_i+H_c)}^{-H_i} 2\sqrt{\left(\frac{V_p(z)}{k_c}\right)^{-2} - p^2}\,dz \quad (9)$$

Where i and j are indexes corresponding to the candidate sedimentary thickness (H_i) and Vp/Vs (k_j); $V_p(z)$ is the P wave velocity at depth z; p is the ray parameter; H_c and k_c are

the sub-sediment crustal thickness and Vp/Vs, respectively, obtained from applying Equation 5.

In order to distinguish the above two kinds of H − k stacking procedures (Equations 5 and 6), in the following we refer the grid-search procedure (Equation 5) to image the subsediment crustal structure as $(H-k)_c$ stacking, and that for the sedimentary structure (Equation 6) as $(H-k)_d$ stacking.

3. Synthetic Experiment

To test the above technique, we generate synthetic RFs using a reflectivity-based method (Randall, 1994) with a Gaussian wavelet of the form $\exp(-4t^2)$. The station is in a sedimentary basin, and the ith hypothetical event has an epicentral distance of 30+i degrees where $i = 0, \cdots 60$. Synthetic RFs are generated using the following parameters: for the sedimentary layer, the thickness, V_p, V_s, V_p/V_s, and density are 0.7 km, 2.1 km/s, 0.7 km/s, 3.0, and 1970 kg/m^3, respectively; for the sub-sediment crustal layer, the corresponding values are 35 km, 6.1 km/s, 3.49 km/s, 1.75, and 2700 kg/m^3; and for the mantle, they are ∞, 8.0 km/s, 4.5 km/s, 1.78, and 3300 kg/m^3. On the synthetic RFs, the Moho Ps phases are completely masked by the strong near surface reverberations (Figure 3a). H− k stacking without considering the sedimentary effects results in incorrect crustal thickness and Vp/Vs (Figure 3c). After applying the resonance-removal filter, PbS and the Moho Ps phases are well recovered (Figure 3d).

The weighting factors in Equations 5 and 6 are selected to maximize the resolution of the resulting optimal thickness and Vp/Vs values, and are dependent on the relative amplitude of the phases involved and the rate of moveout with respect to the

epicentral distance. For investigating the sub-sediment crustal structure, they are set as $\omega_1 = 0.5$, $\omega_2 = 0.4$ and $\omega_3 = 0.1$, and those for imaging the sedimentary structure, the selected values are $\omega_4 = 0.05$, $\omega_2 = 0.7$ and $\omega_3 = 0.25$. Ten bootstrap iterations are used to evaluate the standard deviations of the observed sedimentary and sub-sediment crustal parameters (Efron and Tibshirani, 1986; Press et al., 1992; Liu and Gao, 2010).

The $(\mathrm{H}-\mathrm{k})_{\mathrm{c}}$ stacking technique is then applied on the filtered RFs to search for the optimal sub-sediment crustal thickness (in the range of 20-55 km with an interval of 0.1 km) and Vp/Vs (in the range of 1.65-1.95 with an interval of 0.01). The resulting subsediment crustal thickness is 35.0 km and the Vp/Vs is 1.78 (Figure 3e), which are nearly identical to the input parameters (35.0 km and 1.75) used to generate the RFs. Similarly, the optimal sedimentary layer thickness and Vp/Vs are searched using the $(\mathrm{H}-\mathrm{k})_{\mathrm{d}}$ stacking procedure in the depth range of 0-4 km with an interval of 0.05 km, and in the Vp/Vs range of 1.50-5.00 with an interval of 0.01. The results are 0.70 km and 2.95, respectively (Figure 3f), which are almost the same as the input parameters of 0.7 km and 3.0. We next use noisy synthetic RFs to further test the techniques. Figure 4 shows results for a model in which the RFs are contaminated by random noise with a peak amplitude of 15% relative to the amplitude of the first peak. H − k stacking using the original RFs fails to obtain the correct results (Figure 4c). After applying the resonance-removal filter, the resulting H and Vp/Vs for the sub-sediment crust (35.8 km and 1.74) and the low-velocity sedimentary layer (0.55 km and 3.68) are similar to the parameters used to generate the noisy RFs (Figures 4e and 4f).

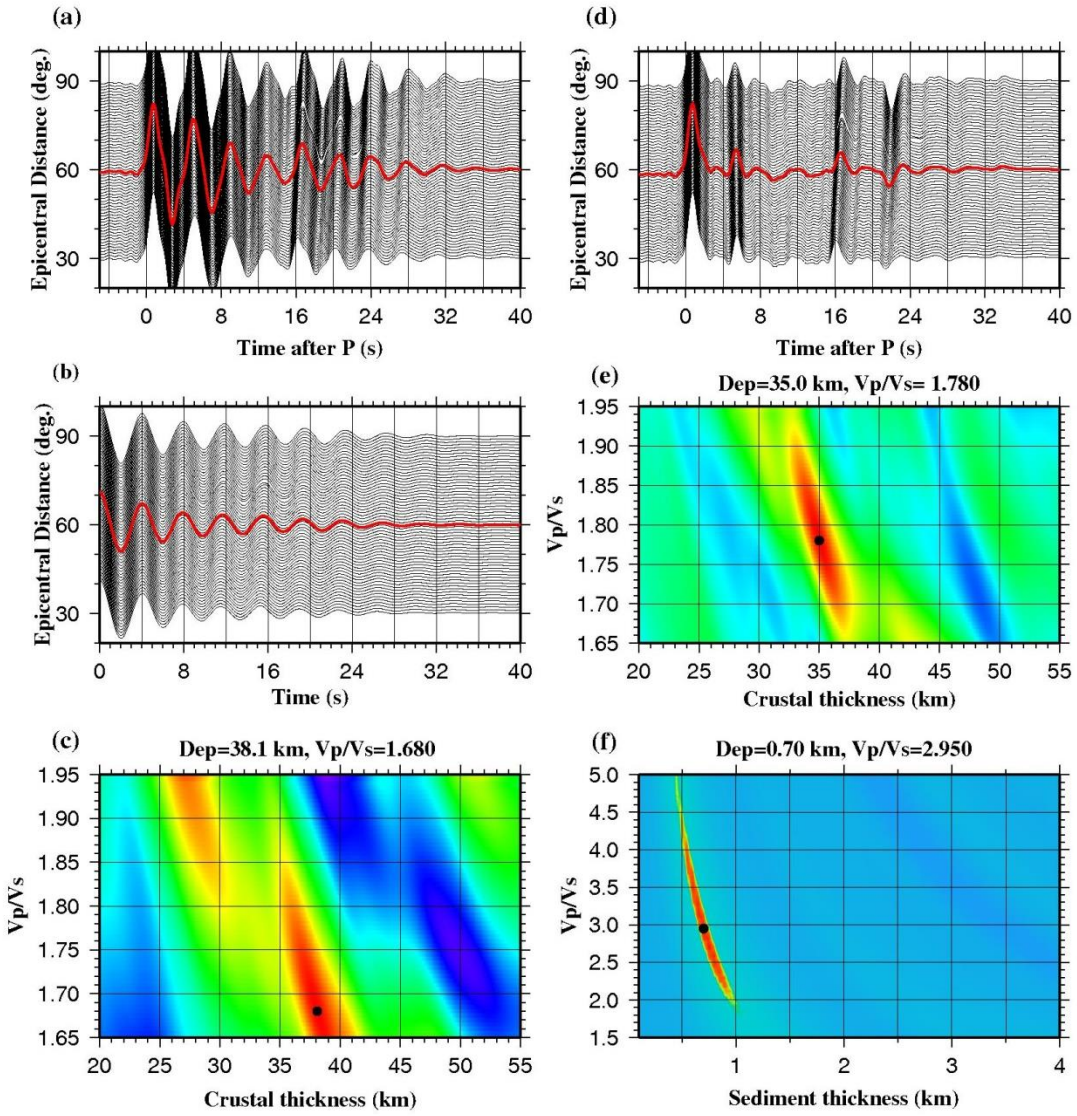

Figure 3. (a) Synthetic RFs plotted against epicentral distance. The red trace is the result of simple time domain summation (without moveout correction) of the individual traces. (b) Auto-correlations of each RFs in (a) against epicentral distance. (c) Contour of stacking energy from H − k stacking using the RFs shown in (a). (d) Resulting RFs after the application of resonance-removal filters. (e) Contour of stacking energy from $(H-k)_c$ stacking using the filtered RFs shown in (d). (f) Same as (e) but for $(H-k)_d$ stacking.

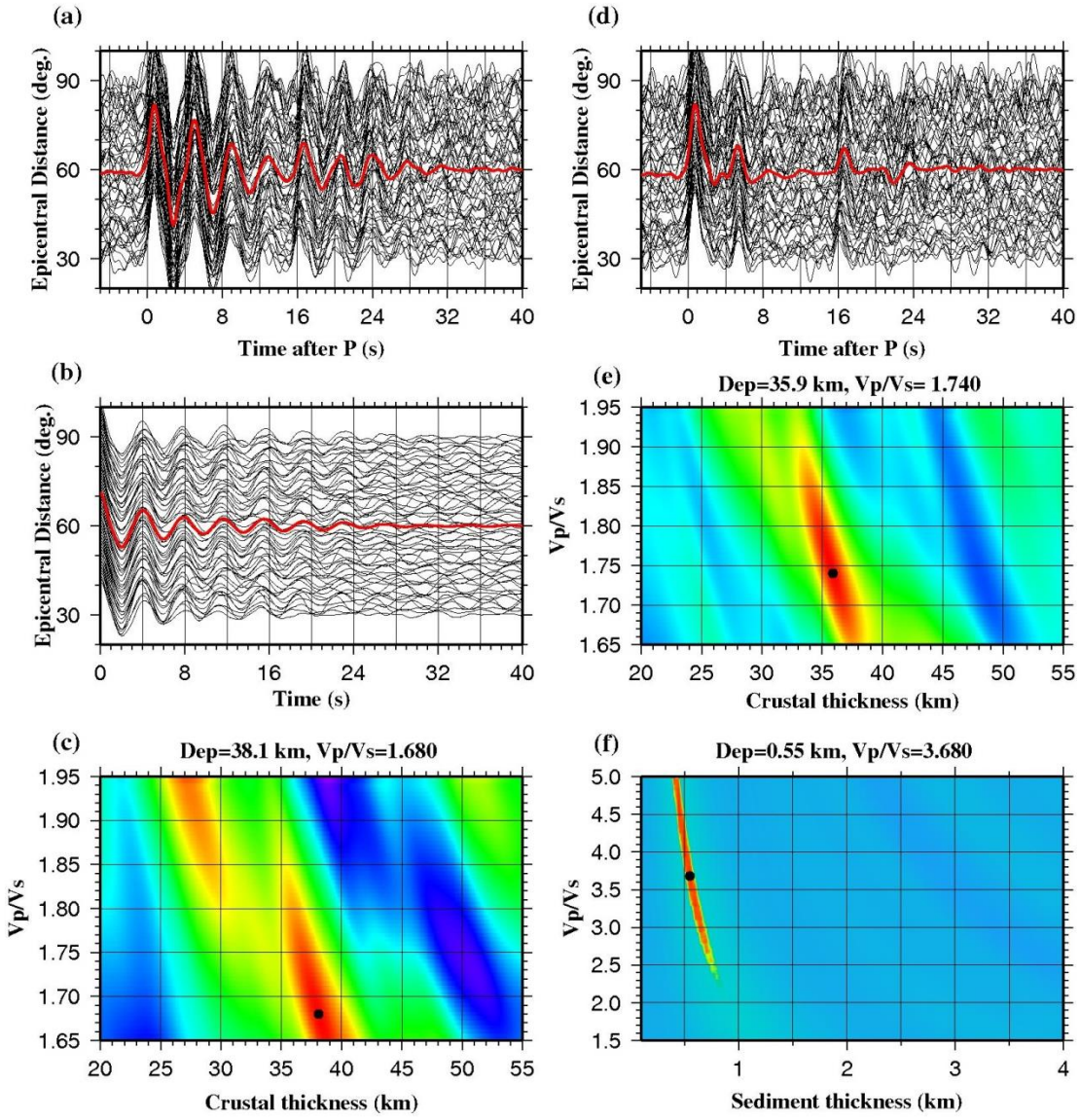

Figure 4. Same as Figure 3 but for a model with 15% random noise added in the RFs.

4. Testing Using Real Data

Our reverberation-removal technique is further tested using RFs recorded by two broadband seismic stations. Station F22A is located in the Powder River Basin, northern Wyoming (USA) and has been studied by Yeck et al. (2013) using the sequential H−k stacking method, and station NE68 is situated in the Songliao Basin, northeast China and has been investigated by Tao et al. (2014) based on the theory of wavefield continuation

and decomposition. The stations were selected because they were used for testing different sediment-removal techniques and also have independent estimates of crustal thickness from active-source seismic experiments.

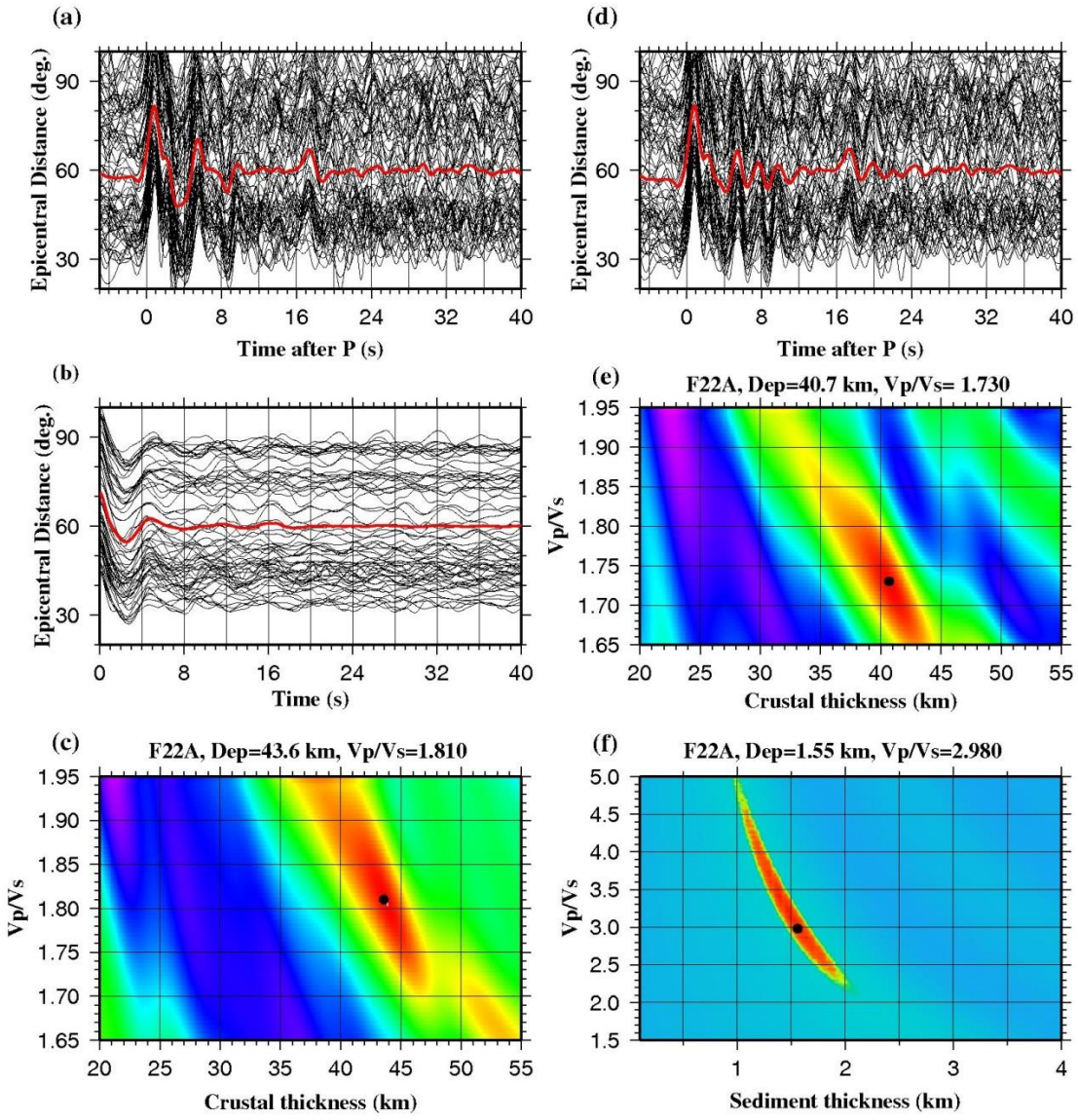

Figure 5. Same as the previous figure but for real data recorded by USArray station F22A located in the Powder River Basin, Wyoming.

Three component data from the stations were requested from the Incorporated Research Institutions for Seismology (IRIS) Data Management Center (DMC).

Earthquakes with epicentral distances in the range of $30\sim90^{\circ}$, and with a magnitude of Mc or greater were used in the study, where Mc is defined as $5.2 + (\Delta - 30.0)/(180.0 - 30.0) - D/700.0$, in which Δ is the epicentral distance in degree, and D is the focal depth in km (Liu and Gao, 2010). The seismograms were windowed at 20 s before and 260 s after the predicted direct P−wave arrival calculated using the IASP91 Earth model. A band-pass filter in the frequency range of 0.04− 0.8 Hz was applied to enhance the signals. An event was not used if the radial component has a signal to noise ratio (SNR) below 4.0. The selected seismograms were converted to radial RFs using the procedure of Ammon (1991), and an SNR-based procedure was applied to reject low-quality RFs. Detailed information about the seismogram and RF selection procedures including the definition of the SNRs can be found in Gao and Liu (2014b).

4.1 Station F22A

For station F22A, we use the same P−wave velocities for the sedimentary and subsediment crustal layers as those used in Yeck et al. (2013), which are 3.6 km/s and 6.7 km/s, respectively. The sedimentary Vp was taken from well logs (Moore, 1985) and the sub-sediment crustal Vp was obtained from nearby active source seismic studies (Snelson et al., 1998). On the original RFs (Figure 5a), there is a strong arrival at about 5 s with an amplitude of about 50% of that of the first peak. In addition, there is a strong trough between this arrival and the first peak. Both arrivals and the well-defined trough on the auto-correlation functions (Figure 5b) indicate the existence of a low-velocity sedimentary layer. After applying the resonance-removal filter to the original 89 RFs (Figure 5a), the Moho Ps phases are well revealed (Figure 5d). Obviously, the strong

amplitude at ~5 s on the original RFs (Figure 5a) are caused by the accidental simultaneous arrival of the PmS and the first positive pulse of the reverberation of the PbS phase.

Application of the $(H-k)_c$ stacking procedure leads to a sub-sedimentary crustal thickness of 40.7±0.2 km and a Vp/Vs of 1.73±0.01 (Figure 5e), which are comparable with the values of 40.5±0.6 km and 1.77±0.01 obtained by Yeck et al. (2013). The obtained subsediment crustal thickness is also consistent with that from active source seismic studies (Snelson et al., 1998), which reported a value of about 40 km. The resulting sedimentary thickness and Vp/Vs are 1.5±0.07 km and 3.13±0.14, respectively (Figure 5f), which are similar to the results of 2.1±0.08 km and 2.54±0.07 reported by Yeck et al. (2013). The slight mismatch between our results and those obtained by Yeck et al. (2013) could be resulted from different approaches and parameters used for data selection, processing, and RF stacking.

4.2 Station NE68

Station NE68 has 362 high-quality RFs with significantly better-developed reverberations than F22A. On the original RFs, the Moho Ps phases are completely masked by the strong near surface reverberations (Figure 6a). Following Tao et al. (2014), we use an average P−wave velocities of 2.1 km/s for the sedimentary layer and 6.4 km/s for the sub-sediment crust. After applying the resonance-removal filter, the near surface reverberations are effectively suppressed, and consequently the Moho Ps phases are clearly observed (Figures 6d). Results from $(H-k)_c$ stacking using the filtered RFs are almost identical to those obtained by Tao et al. (2014), who reported a sub-sediment

crustal thickness of 35.0 km and Vp/Vs of 1.730, and our $(H-k)_d$ stacking yields 35.2 ± 0.2 km and 1.74 ± 0.01 (Figure 6e), respectively. Similarly, the resulting sedimentary thickness and Vp/Vs using $(H-k)_d$ stacking are 0.35 ± 0.00 km and 4.61 ± 0.02 (Figure 6f), which are consistent with those obtained by Tao et al. (2014) (0.31 km and 4.118). The observed thickness of the low-velocity sedimentary layer also agrees well with results from an active source seismic experiment (Feng et al., 2010).

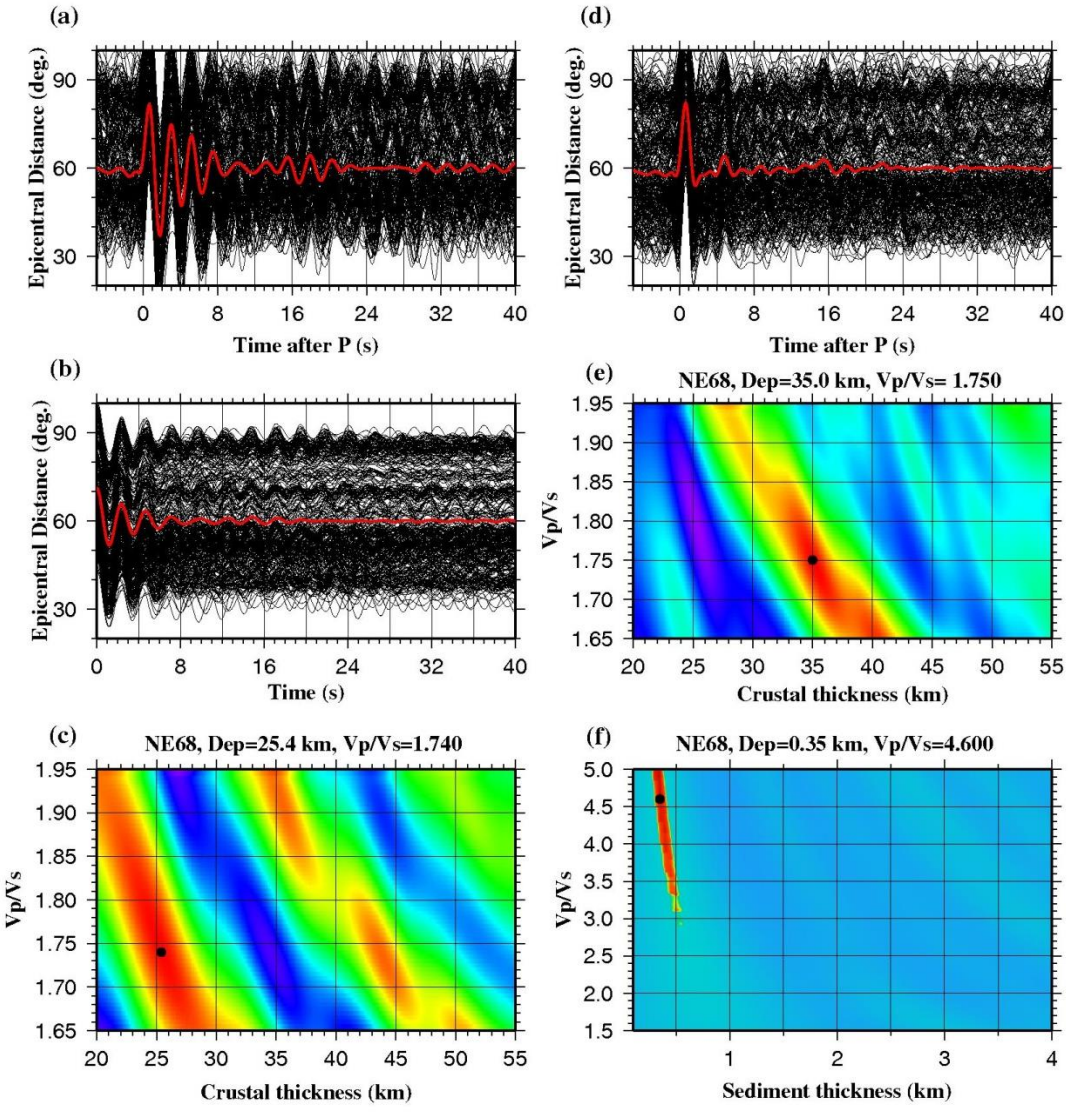

Figure 6. Same as the previous figure but for station NE68 in the Songliao Basin, northeast China.

5. Discussion and Conclusion

The resulting high Vp/Vs values for stations NE68 and F22A can be caused by a poorly consolidated sedimentary layer. Very high Vp/Vs of such a layer has been observed elsewhere. For instance, beneath the Horn River Basin in Northeast British Columbia, Canada, well-logging and active-source seismic data revealed high Vp/Vs values ranging from about 2.5 to 5.5 in the top 500 m of the basin (see Figures 4 and 5 in Zuleta-Tobon, 2012). Laboratory experiments (Prasad et al., 2004) indicate that Vp/Vs values are related to water content, amount of clay minerals, and the overlying pressure. The high sedimentary Vp/Vs values observed at stations NE68 and F22A suggest water saturation, high clay content, and perhaps low overlying pressure in the Songliao and Powder River Basins.

The strong reverberations in the radial RFs caused by a low-velocity sedimentary layer can be effectively removed by applying the resonance-removal filter to decipher the Ps phases associated with the Moho and the P-to-S converted phase from the bottom of the sedimentary layer. Tests using synthetic and real data indicate that the proposed technique can efficiently obtain the thickness and Vp/Vs of both the sedimentary layer and the sub-sediment crust with high reliability. Contrary to most other techniques, which favor the absence or weak sedimentary reverberations, the proposed technique leads to more accurately determined results with stronger reverberations, thanks to the better-defined parameters needed by the resonance-removal filter associated with stronger reverberations. Also, the technique is computationally inexpensive and thus can be applied to large data sets such as those recorded by the USArray.

Obviously, the existence of strong reverberations of at least a couple of cycles is needed in order for the proposed technique to be applied successfully. Testing using data from numerous stations suggests that as long as the RFs have reverberations with a dominant frequency, the technique can successfully remove the reverberations. Such reverberations cannot be generated if the sedimentary layer is thinner than about 1/4 of the wavelength of the PbS phase. If we assume a sedimentary S−wave velocity of 0.33 km/s and a period of 3 s, the required minimum thickness is about 0.25 km. On the other hand, if the sedimentary layer is too thick (e.g., thicker than 5-8 km, depending on the attenuation factor), the reverberations decay rapidly with time, leading to poorly defined resonance-removal filters. A thick sedimentary layer is characterized by RFs with abnormally low frequencies and a large delay of the PbS phase. Another potential problem for a very thick sedimentary layer is that the impedance contrast across the basin bottom may be too small (due to gravitational compaction) to generate significant reverberations. Furthermore, the technique is not expected to perform well if there are strong interfaces inside the sedimentary layer. Such interfaces produce complicated interactions between the reverberations in two or more layers, and modifications to Equation 2 and other steps of the technique are needed to account for such scenario. Finally, cautions must be taken for stations near the edge of sedimentary basins or in areas with significant undulations of the basin bottom. Due to the rapid lateral variation in the thickness of the sedimentary layer, the two-way travel-time of the reverberations could be dependent on the arriving direction of the seismic waves. In such a case the above technique can be applied to events from narrow azimuthal bands.

SECTION

2. CONCLUSIONS

In this study, the recently archived broadband seismic data in the vicinity of the ORZ were employed to conduct the first receiver function study of mantle transition zone discontinuities and SWS investigation of the incipient rift. The apparently shallower-than-normal MTZ discontinuities observed beneath the Kalahari Craton can be explained by the existence of a lithosphere that is 100-150 km thicker than that beneath the Congo Craton and the Damara belt. The resulting mantle anisotropy shows a dominantly NE-SW orientation which is parallel to the African APM. Although significant contributions from the lithosphere to the observed anisotropy cannot be completely ruled out, spatial coherency analysis of the splitting parameters and correspondence with geological features suggest that the center of the approximately 120 km thick anisotropic layer is located between the depth of 240 and 280 km, implying an asthenospheric origin of anisotropy, probably as the result of simple shear in the boundary layer between the lithosphere and the asthenosphere (Fig. 2.1). Comparison of the resulting SWS measurements with predicted mantle flow directions originating from an active mantle plume or edge-driven small-scale mantle convection suggests that neither is operating beneath the incipient rift, which is supported by the absence of significant delays in teleseismic P- and S-wave travel-time residuals beneath the ORZ. A new model of continental rifting was proposed, in which differential basal drag applied to cratonic blocks results in relative intra-plate movements and leads to rifting along ancient orogenic zones, which are areas of mechanical weakness. The ORZ is possibly initiated

by the relative movements between Congo and Kalahari cratons along the weak zones of Damara belts.

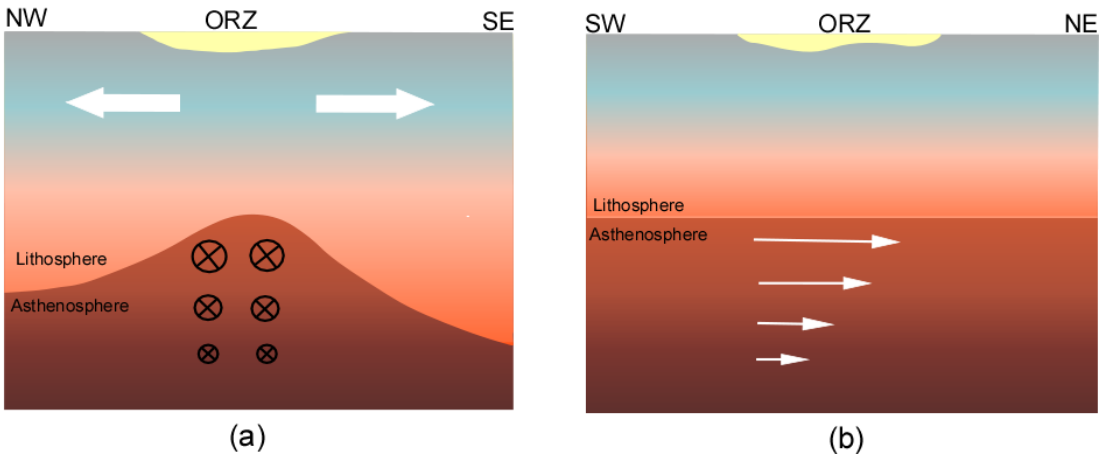

Figure 2.1 Schematic cross sections of (a) traversing and (b) along the Okavango Rift zone demonstrating the mechanism of shearing between the lithosphere and asthenosphere. The white arrows in (a) indicate the opening of the ORZ and the circles filled with pluses represent the flowing direction of going inside. The white arrows in (b) are corresponding to the direction of the mantle flow and their lengths are proportional to the strength of the anisotropy.

The strong reverberations in the radial RFs caused by a low-velocity sedimentary layer can be effectively removed by applying the resonance-removal filter to decipher the Ps phases associated with the Moho and the P-to-S converted phase from the bottom of the sedimentary layer. Tests using synthetic and real data indicate that the proposed technique can efficiently obtain the thickness and Vp/Vs of both the sedimentary layer and the sub-sediment crust with high reliability. Contrary to most other techniques, which favor the absence or weak sedimentary reverberations, the proposed technique leads to more accurately determined results with stronger reverberations, thanks to the better-defined parameters needed by the resonance-removal filter associated with stronger reverberations. Also, the technique is computationally inexpensive and thus can be applied to large data sets such as those recorded by the USArray.

APPENDIX

Individual shear wave splitting measurements for the 22 stations used in this day

Station			Phase	SWS parameters				Event				Rank
Name	Lat.	Long.		θ	STD θ	δt	STD δt	BAZ	Lat.	Long.	Depth	
B01KRx_XK	-22.24	26.72	SKS	31	1.5	1.4	0.17	44.0	49.8	145.1	583	A
B01KRx_XK	-22.24	26.72	SKS	30	18	0.85	0.35	91.8	2.2	126.8	91	B
B01KRx_XK	-22.24	26.72	SKS	49	6	1.75	0.38	348.7	71.4	-10.6	14	B
B01KRx_XK	-22.24	26.72	SKS	49	6.5	0.7	0.1	266.8	1.9	-76.4	170	B
B01KRx_XK	-22.24	26.72	SKS	59	4.5	1	0.12	269.8	5.8	-78.2	12	B
B01KRx_XK	-22.24	26.72	SKS	38	15.5	0.9	0.3	280.4	10.9	-62.3	63	B
B01KRx_XK	-22.24	26.72	SKS	77	5.5	0.85	0.15	286.4	19.0	-66.8	20	B
B01KRx_XK	-22.24	26.72	SKS	17	9.5	1.1	0.22	248.9	-20.0	-70.8	3	B
B02LTx_XK	-21.39	25.58	SKS	55	14	1.1	0.38	83.8	10.8	126.6	28	B
B02LTx_XK	-21.39	25.58	SKS	52	8	1.25	0.25	99.2	-4.5	129.1	10	B
B02LTx_XK	-21.39	25.58	SKS	62	2.5	1.25	0.15	85.1	9.2	126.2	37	B
B02LTx_XK	-21.39	25.58	SKS	63	4	0.9	0.1	101.4	-6.5	129.8	155	A
B02LTx_XK	-21.39	25.58	SKS	52	18.5	0.8	0.5	93.4	0.6	126.2	30	B
B02LTx_XK	-21.39	25.58	SKS	50	6.5	0.75	0.1	266.3	1.1	-77.4	145	A
B02LTx_XK	-21.39	25.58	SKS	53	5	1.05	0.15	81.2	18.7	145.3	602	A
B02LTx_XK	-21.39	25.58	SKS	70	13.5	1.1	0.38	110.0	-6.0	149.7	62	B
B02LTx_XK	-21.39	25.58	SKS	59	15	0.85	0.25	101.6	-7.4	128.2	112	B
B03SLx_XK	-21.12	24.76	SKS	16	6	0.9	0.15	43.3	49.8	145.1	583	B
B03SLx_XK	-21.12	24.76	SKS	27	4.5	1.05	0.15	51.8	42.7	131.1	562	A
B03SLx_XK	-21.12	24.76	SKS	57	12	0.9	0.32	81.3	18.7	145.3	602	B
B03SLx_XK	-21.12	24.76	SKS	31	5	1.15	0.22	54.4	34.5	104.2	10	B
B03SLx_XK	-21.12	24.76	SKS	175	5	1.45	0.35	249.5	-20.0	-70.8	3	B
B03SLx_XK	-21.12	24.76	SKS	14	5.5	0.75	0.1	149.9	-24.6	179.1	527	B
B04KHx_XK	-20.47	24.51	SKS	33	12	0.65	0.17	89.5	4.2	124.5	326	B

B04KHx_XK	-20.47	24.51	SKS	172	13.5	0.8	0.25	240.9	-29.1	-71.2	63	B
B04KHx_XK	-20.47	24.51	SKS	25	2.5	1.6	0.12	51.6	42.7	131.1	562	B
B04KHx_XK	-20.47	24.51	SKS	40	5	1.2	0.18	80.9	18.7	145.3	602	B
B04KHx_XK	-20.47	24.51	SKS	21	8	0.65	0.1	156.1	-41.7	174.4	14	B
B04KHx_XK	-20.47	24.51	SKS	18	7	1.45	0.22	54.5	34.5	104.2	10	B
B04KHx_XK	-20.47	24.51	SKS	176	7.5	1.85	0.33	56.4	30.0	98.0	6	B
B04KHx_XK	-20.47	24.51	SKS	22	6	1.45	0.22	66.7	29.9	138.8	402	B
B04KHx_XK	-20.47	24.51	SKS	12	10.5	1.4	0.32	249.6	-20.0	-70.8	3	B
B04KHx_XK	-20.47	24.51	SKS	17	9.5	1	0.22	149.9	-24.6	179.1	527	B
B05MOx_XK	-20.22	24.13	SKS	2	13	1.2	0.43	259.2	-8.4	-74.3	145	B
B05MOx_XK	-20.22	24.13	SKS	45	16.5	0.55	0.22	85.3	9.2	126.2	37	B
B05MOx_XK	-20.22	24.13	SKS	25	15	1.15	0.48	51.5	42.7	131.1	562	A
B05MOx_XK	-20.22	24.13	SKS	30	5	1.3	0.23	58.0	30.3	102.9	14	B
B05MOx_XK	-20.22	24.13	SKS	30	7.5	1.25	0.3	54.6	34.5	104.2	10	B
B05MOx_XK	-20.22	24.13	SKS	47	6.5	1.45	0.22	274.5	11.6	-85.9	135	B
B06ORx_XK	-19.9	23.53	SKS	72	4	1.6	0.33	92.5	2.2	126.8	91	B
B06ORx_XK	-19.9	23.53	SKS	43	15	0.6	0.17	89.7	4.2	124.5	326	B
B06ORx_XK	-19.9	23.53	SKS	56	17	0.85	0.35	258.8	-8.9	-75.1	129	B
B06ORx_XK	-19.9	23.53	SKS	27	4	1	0.15	51.4	42.7	131.1	562	A
B06ORx_XK	-19.9	23.53	SKS	38	9.5	1.15	0.45	54.8	34.5	104.2	10	B
B06ORx_XK	-19.9	23.53	SKS	34	6	1.4	0.4	287.8	19.0	-66.8	20	B
B07DXx_XK	-20.55	22.75	SKS	76	16	0.7	0.18	102.3	-6.5	129.8	155	B
B07DXx_XK	-20.55	22.75	SKS	61	12.5	0.9	0.32	81.4	18.7	145.3	602	B
B08TSx_XK	-20.16	22.46	SKS	27	8	1.05	0.45	102.4	-6.5	129.8	155	B
B10PPx_XK	-18.91	22.54	SKS	26	2.5	1.6	0.2	41.9	49.8	145.1	583	B
B10PPx_XK	-18.91	22.54	SKS	36	16	1.1	0.43	56.6	37.9	143.9	31	B
B10PPx_XK	-18.91	22.54	SKS	17	8	0.9	0.15	51.1	42.7	131.1	562	A
B11ETx_XK	-19.02	22.32	SKS	12	11	1.05	0.25	56.6	37.9	143.9	31	B
B11ETx_XK	-19.02	22.32	SKS	176	15.5	0.9	0.32	66.1	29.9	138.8	402	B

B11ETx_XK	-19.02	22.32	SKS	38	14.5	1.15	0.4	282.0	10.9	-62.3	63	B
B12SSx_XK	-18.75	22.2	SKS	76	15	0.75	0.3	288.3	19.0	-66.8	20	B
B13NXx_XK	-18.58	21.99	SKS	61	18.5	0.8	0.33	260.3	-5.4	-81.9	10	B
B15MWx_XK	-19.63	23.83	SKS	26	6.5	1.4	0.58	42.5	49.8	145.1	583	B
B15MWx_XK	-19.63	23.83	SKS	50	16	0.6	0.22	101.7	-6.5	129.8	155	A
B15MWx_XK	-19.63	23.83	SKS	28	8	1	0.25	51.3	42.7	131.1	562	A
B15MWx_XK	-19.63	23.83	SKS	55	6	1.4	0.3	80.5	18.7	145.3	602	B
B17CIx_XK	-19.29	22.91	SKS	43	5	0.9	0.12	259.7	-8.4	-74.3	145	A
B17CIx_XK	-19.29	22.91	SKS	22	11	0.55	0.15	259.0	-8.9	-75.1	129	A
B17CIx_XK	-19.29	22.91	SKS	1	6	1	0.2	54.9	34.5	104.2	10	B
SA64xx_XA	-22.97	26.2	SKS	60	18.5	0.75	0.48	279.8	10.6	-63.5	19	B
SA64xx_XA	-22.97	26.2	SKS	75	2	1.3	0.15	268.9	3.9	-75.8	198	A
SA64xx_XA	-22.97	26.2	SKS	33	16.5	0.5	0.17	255.5	-13.7	-68.8	586	B
SA65xx_XA	-22.82	27.22	SKS	31	7.5	1.2	0.32	136.4	-20.4	169.3	57	B
SA65xx_XA	-22.82	27.22	SKS	76	3	1.25	0.3	268.5	3.9	-75.8	198	A
SA65xx_XA	-22.82	27.22	SKS	40	5	1.15	0.18	94.4	-3.8	119.7	33	B
SA66xx_XA	-21.90	26.37	SKS	65	18.5	1.2	0.47	279.9	10.6	-63.5	19	B
SA66xx_XA	-21.90	26.37	SKS	71	3	1.3	0.2	269.1	3.9	-75.8	198	A
SA66xx_XA	-21.90	26.37	SKS	60	17	1.15	0.48	261.0	-4.4	-76.7	112	B
SA66xx_XA	-21.90	26.37	SKS	62	3.5	1	0.2	255.4	-13.7	-68.8	586	B
SA66xx_XA	-21.90	26.37	SKS	67	9	1.05	0.28	269.1	3.9	-75.8	177	B
SA66xx_XA	-21.90	26.37	SKS	82	13.5	0.85	0.28	108.3	-5.5	147.9	179	B
SA66xx_XA	-21.90	26.37	SKS	46	16	0.9	0.28	74.6	23.9	141.9	95	B
SA67xx_XA	-21.89	27.27	SKS	69	3.5	1.3	0.15	279.5	10.6	-63.5	19	B
SA67xx_XA	-21.89	27.27	SKS	61	12	0.85	0.22	268.7	3.9	-75.8	198	A
SA67xx_XA	-21.89	27.27	SKS	55	5	1.25	0.25	255.1	-13.7	-68.8	586	B
SA67xx_XA	-21.89	27.27	SKS	66	9.5	1	0.23	268.8	3.9	-75.8	177	B
SA67xx_XA	-21.89	27.27	SKS	60	11.5	0.85	0.25	273.8	14.4	-91.5	33	B
SA70xx_XA	-21.09	26.34	SKS	34	11	1	0.25	82.4	10.2	121.7	33	B

SA70xx_XA	-21.09	26.34	SKS	45	2.5	1.15	0.15	153.7	-32.1	179.8	332	A
SA70xx_XA	-21.09	26.34	SKS	58	3	1.1	0.1	269.3	3.9	-75.8	198	A
SA70xx_XA	-21.09	26.34	SKS	59	11.5	1	0.25	175.2	-63.1	-164.3	10	B
SA70xx_XA	-21.09	26.34	SKS	49	7	1.45	0.27	84.1	9.8	125.8	105	B
SA70xx_XA	-21.09	26.34	SKS	57	12.5	0.85	0.25	261.2	-4.4	-76.7	112	B
SA70xx_XA	-21.09	26.34	SKS	36	11	1.05	0.3	91.1	1.2	122.5	24	B
SA70xx_XA	-21.09	26.34	SKS	53	12	1.3	0.5	255.4	-13.7	-68.8	586	A
SA70xx_XA	-21.09	26.34	SKS	69	4	1.05	0.2	269.3	3.9	-75.8	177	B
SA70xx_XA	-21.09	26.34	SKS	74	12	0.8	0.17	108.0	-5.5	147.9	179	B
SA70xx_XA	-21.09	26.34	SKS	44	8.5	0.8	0.2	74.1	23.9	141.9	95	B
B01KRx_XK	-22.24	26.72	PKS	33	1	1.8	0.17	43.1	49.3	155.4	29	B
B01KRx_XK	-22.24	26.72	PKS	21	1	1.9	0.13	34.2	54.7	162.3	43	B
B01KRx_XK	-22.24	26.72	PKS	49	11.5	0.6	0.13	274.1	17.2	-100.7	17	A
B02LTx_XK	-21.39	25.58	PKS	57	12.5	1	0.3	25.8	51.6	-178.3	16	B
B02LTx_XK	-21.39	25.58	PKS	40	12	0.95	0.27	276.6	18.3	-100.4	53	B
B02LTx_XK	-21.39	25.58	PKS	49	3	1.15	0.2	125.7	-10.9	166.0	21	B
B02LTx_XK	-21.39	25.58	PKS	49	9.5	0.7	0.13	275.3	17.4	-101.0	24	B
B03SLx_XK	-21.12	24.76	PKS	12	3.5	0.9	0.1	42.0	49.3	155.4	29	B
B03SLx_XK	-21.12	24.76	PKS	19	5	0.9	0.18	39.3	50.9	157.3	41	B
B03SLx_XK	-21.12	24.76	PKS	10	11.5	0.95	0.28	39.2	50.9	157.5	41	B
B03SLx_XK	-21.12	24.76	PKS	19	7	0.9	0.2	39.2	50.9	157.4	29	A
B03SLx_XK	-21.12	24.76	PKS	17	7	1.5	0.4	40.4	50.1	157.2	18	B
B03SLx_XK	-21.12	24.76	PKS	1	14.5	0.75	0.28	36.7	52.2	160.2	18	B
B03SLx_XK	-21.12	24.76	PKS	19	1	0.9	0.07	39.2	52.2	151.5	623	A
B03SLx_XK	-21.12	24.76	PKS	20	1.5	0.9	0.1	37.7	53.2	152.8	580	A
B03SLx_XK	-21.12	24.76	PKS	15	5	0.75	0.15	32.9	54.7	162.3	43	A
B03SLx_XK	-21.12	24.76	PKS	31	3	1.25	0.25	133.2	-14.7	169.8	638	B
B04KHx_XK	-20.47	24.51	PKS	11	15	0.85	0.32	130.8	-14.7	167.3	160	B
B04KHx_XK	-20.47	24.51	PKS	23	2.5	1.65	0.2	41.5	49.3	155.4	29	A

B04KHx_XK	-20.47	24.51	PKS	14	6.5	0.7	0.12	130.4	-14.3	167.3	188	A
B04KHx_XK	-20.47	24.51	PKS	24	2	1.6	0.17	38.8	50.9	157.3	41	A
B04KHx_XK	-20.47	24.51	PKS	16	2.5	2.05	0.23	38.8	50.9	157.5	41	B
B04KHx_XK	-20.47	24.51	PKS	21	1.5	1.7	0.13	38.8	50.9	157.4	29	A
B04KHx_XK	-20.47	24.51	PKS	11	7.5	1.05	0.27	80.9	18.7	145.3	602	B
B04KHx_XK	-20.47	24.51	PKS	28	3.5	1	0.1	152.9	-23.0	-177.1	171	A
B04KHx_XK	-20.47	24.51	PKS	26	6.5	1.6	0.25	152.8	-20.6	-175.8	149	B
B04KHx_XK	-20.47	24.51	PKS	18	1.5	1.6	0.1	38.8	52.2	151.5	623	A
B04KHx_XK	-20.47	24.51	PKS	18	2.5	1.65	0.17	37.3	53.2	152.8	580	A
B04KHx_XK	-20.47	24.51	PKS	23	2	1.9	0.22	32.4	54.7	162.3	43	B
B04KHx_XK	-20.47	24.51	PKS	28	6	0.9	0.2	329.5	49.8	-127.4	11	B
B05MOx_XK	-20.22	24.13	PKS	12	3	0.85	0.08	41.2	49.3	155.4	29	A
B05MOx_XK	-20.22	24.13	PKS	16	11.5	0.75	0.2	38.6	50.9	157.3	41	B
B05MOx_XK	-20.22	24.13	PKS	22	9	0.6	0.17	38.5	50.9	157.4	29	B
B05MOx_XK	-20.22	24.13	PKS	6	14	0.65	0.18	153.2	-23.0	-177.1	171	B
B05MOx_XK	-20.22	24.13	PKS	18	9.5	0.75	0.18	156.4	-24.3	-174.9	10	B
B05MOx_XK	-20.22	24.13	PKS	15	2	0.65	0.07	38.6	52.2	151.5	623	A
B05MOx_XK	-20.22	24.13	PKS	21	6.5	0.6	0.2	37.1	53.2	152.8	580	B
B06ORx_XK	-19.9	23.53	PKS	27	1.5	1.4	0.23	38.1	50.9	157.4	29	B
B06ORx_XK	-19.9	23.53	PKS	22	7	1.55	0.32	137.3	-19.1	169.5	280	B
B06ORx_XK	-19.9	23.53	PKS	21	2	1.15	0.13	38.3	52.2	151.5	623	A
B06ORx_XK	-19.9	23.53	PKS	24	5	1.3	0.45	36.8	53.2	152.8	580	B
B07DXx_XK	-20.55	22.75	PKS	63	6.5	1.25	0.33	132.3	-14.7	167.3	160	B
B07DXx_XK	-20.55	22.75	PKS	52	2.5	1.3	0.25	132.0	-14.3	167.3	188	B
B07DXx_XK	-20.55	22.75	PKS	56	5	1.45	0.38	127.5	-10.6	166.4	9	B
B07DXx_XK	-20.55	22.75	PKS	52	4	1.5	0.48	131.5	-13.9	167.2	187	B
B08TSx_XK	-20.16	22.46	PKS	57	2	1.75	0.25	132.4	-14.7	167.3	160	B
B08TSx_XK	-20.16	22.46	PKS	66	8	1.25	0.33	129.5	-12.5	166.5	27	B
B08TSx_XK	-20.16	22.46	PKS	57	2.5	1.2	0.17	132.0	-14.3	167.3	188	A

B08TSx_XK	-20.16	22.46	PKS	63	3	1.35	0.18	129.1	-12.1	166.5	112	B
B10PPx_XK	-18.91	22.54	PKS	17	7	1.05	0.2	40.0	49.3	155.4	29	A
B10PPx_XK	-18.91	22.54	PKS	14	4	1.5	0.25	34.4	52.4	160.4	14	B
B10PPx_XK	-18.91	22.54	PKS	25	3	1.85	0.38	37.6	52.2	151.5	623	A
B10PPx_XK	-18.91	22.54	PKS	49	10	1	0.25	113.7	-6.4	154.9	35	B
B10PPx_XK	-18.91	22.54	PKS	36	15	0.8	0.33	155.5	-24.0	-176.7	64	B
B12SSx_XK	-18.75	22.2	PKS	87	6.5	1.35	0.23	27.0	57.6	163.2	10	B
B12SSx_XK	-18.75	22.2	PKS	65	10.5	1.3	0.55	41.8	49.8	145.1	583	B
B12SSx_XK	-18.75	22.2	PKS	86	9	0.55	0.1	126.5	-11.7	164.9	8	B
B13NXx_XK	-18.58	21.99	PKS	51	3	1.7	0.28	34.2	52.2	160.2	18	B
B14MHx_XK	-18.3	21.79	PKS	15	15.5	0.65	0.2	126.5	-11.7	164.9	8	B
B15MWx_XK	-19.63	23.83	PKS	8	6.5	1.4	0.23	40.5	49.4	156.1	10	B
B15MWx_XK	-19.63	23.83	PKS	21	3.5	1.15	0.18	40.8	49.3	155.4	29	A
B15MWx_XK	-19.63	23.83	PKS	21	8	1	0.35	38.1	50.9	157.3	41	B
B15MWx_XK	-19.63	23.83	PKS	16	6	1	0.23	38.1	50.9	157.4	29	B
B15MWx_XK	-19.63	23.83	PKS	15	6.5	1.1	0.3	35.3	52.4	160.4	14	B
B15MWx_XK	-19.63	23.83	PKS	11	3	0.95	0.1	38.3	52.2	151.5	623	A
B1665x_XK	-22.82	27.23	PKS	13	20.5	0.35	0.18	40.6	52.2	151.5	623	B
B1665x_XK	-22.82	27.23	PKS	28	5	0.65	0.22	39.1	53.2	152.8	580	B
B1665x_XK	-22.82	27.23	PKS	73	9	0.7	0.18	273.4	17.2	-100.7	17	B
B17CIx_XK	-19.29	22.91	PKS	15	6.5	0.9	0.2	40.3	49.3	155.4	29	B
SA66xx_XA	-21.9	26.37	PKS	72	4	1.15	0.15	276.1	18.7	-101.6	70	B
SA67xx_XA	-21.89	27.27	PKS	45	9	0.7	0.12	275.8	18.7	-101.6	70	A
SA70xx_XA	-21.09	26.34	PKS	61	4	0.9	0.1	276.8	18.7	-101.6	70	A
SA70xx_XA	-21.09	26.34	PKS	41	6	1.15	0.33	150.9	-22.1	-176.8	167	B
B01KRx_XK	-22.24	26.72	SKK	44	13.5	0.65	0.2	91.8	2.2	126.8	91	B
B01KRx_XK	-22.24	26.72	SKK	41	6.5	1	0.12	273.2	14.0	-91.9	24	B
B01KRx_XK	-22.24	26.72	SKK	44	5.5	1.4	0.33	58.5	37.9	143.9	31	B
B01KRx_XK	-22.24	26.72	SKK	56	16	1	0.43	79.5	20.8	146.8	9	B

B02LTx_XK	-21.39	25.58	SKK	31	18.5	0.95	0.4	274.1	14.0	-91.9	24	B
B02LTx_XK	-21.39	25.58	SKK	62	7	0.95	0.15	108.2	-7.2	144.0	10	B
B02LTx_XK	-21.39	25.58	SKK	18	10	1	0.25	47.2	46.2	150.8	112	B
B02LTx_XK	-21.39	25.58	SKK	57	1.5	1.5	0.08	81.2	18.7	145.3	602	A
B02LTx_XK	-21.39	25.58	SKK	52	8.5	1.25	0.28	79.2	20.8	146.8	9	B
B02LTx_XK	-21.39	25.58	SKK	54	4.5	1.65	0.55	132.6	-14.7	169.8	638	B
B03SLx_XK	-21.12	24.76	SKK	26	4.5	0.85	0.15	43.3	49.8	145.1	583	A
B03SLx_XK	-21.12	24.76	SKK	35	7.5	1.5	0.38	57.9	37.9	143.9	31	B
B03SLx_XK	-21.12	24.76	SKK	55	4	0.95	0.15	81.3	18.7	145.3	602	A
B03SLx_XK	-21.12	24.76	SKK	24	5.5	1.1	0.28	37.7	53.2	152.8	580	B
B03SLx_XK	-21.12	24.76	SKK	43	6.5	1.6	0.33	67.6	27.4	127.4	119	A
B04KHx_XK	-20.47	24.51	SKK	27	2.5	1.45	0.18	42.9	49.8	145.1	583	A
B04KHx_XK	-20.47	24.51	SKK	41	5	2.1	0.47	57.5	37.9	143.9	31	B
B04KHx_XK	-20.47	24.51	SKK	35	5	0.8	0.08	80.9	18.7	145.3	602	A
B04KHx_XK	-20.47	24.51	SKK	15	7	0.8	0.12	152.9	-23.0	-177.1	171	B
B04KHx_XK	-20.47	24.51	SKK	22	2.5	1.95	0.15	37.3	53.2	152.8	580	B
B04KHx_XK	-20.47	24.51	SKK	35	10	1.55	0.5	67.4	27.4	127.4	119	B
B04KHx_XK	-20.47	24.51	SKK	12	4	0.75	0.08	149.9	-24.6	179.1	527	A
B04KHx_XK	-20.47	24.51	SKK	8	10	1	0.28	149.9	-25.8	178.2	634	A
B05MOx_XK	-20.22	24.13	SKK	2	18.5	0.4	0.25	42.8	49.8	145.1	583	B
B05MOx_XK	-20.22	24.13	SKK	29	9	0.65	0.12	80.8	18.7	145.3	602	A
B05MOx_XK	-20.22	24.13	SKK	48	10.5	1.05	0.27	110.1	-6.0	149.7	62	B
B06ORx_XK	-19.90	23.53	SKK	53	8	1.2	0.27	80.7	18.7	145.3	602	A
B06ORx_XK	-19.90	23.53	SKK	47	4	1.3	0.23	153.7	-23.0	-177.1	171	B
B06ORx_XK	-19.90	23.53	SKK	41	13	1.15	0.33	78.6	20.8	146.8	9	B
B06ORx_XK	-19.90	23.53	SKK	42	4	1.2	0.25	150.7	-24.6	179.1	527	A
B06ORx_XK	-19.90	23.53	SKK	27	11.5	1	0.25	150.6	-25.8	178.2	634	B
B07DXx_XK	-20.55	22.75	SKK	55	21.5	0.6	0.28	81.4	18.7	145.3	602	B
B07DXx_XK	-20.55	22.75	SKK	22	8	1.05	0.2	67.8	27.4	127.4	119	B

B08TSx_XK	-20.16	22.46	SKK	53	12.5	1	0.35	111.0	-6.0	149.7	62	B
B08TSx_XK	-20.16	22.46	SKK	72	1	1.8	0.15	151.9	-24.6	179.1	527	A
B09NKx_XK	-19.66	22.19	SKK	21	9.5	1.1	0.3	155.1	-23.0	-177.2	155	B
B09NKx_XK	-19.66	22.19	SKK	44	13	1.45	0.52	67.6	27.4	127.4	119	B
B09NKx_XK	-19.66	22.19	SKK	27	11	0.9	0.22	156.7	-20.8	-174.7	45	B
B10PPx_XK	-18.91	22.54	SKK	27	8.5	1.15	0.38	41.9	49.8	145.1	583	B
B10PPx_XK	-18.91	22.54	SKK	18	7	0.7	0.13	80.3	18.7	145.3	602	A
B10PPx_XK	-18.91	22.54	SKK	2	5	1.4	0.28	67.2	27.4	127.4	119	B
B11ETx_XK	-19.02	22.32	SKK	24	10.5	0.65	0.15	67.3	27.4	127.4	119	B
B13NXx_XK	-18.58	21.99	SKK	18	12.5	0.5	0.18	80.1	18.7	145.3	602	B
B15MWx_XK	-19.63	23.83	SKK	42	4.5	1.15	0.12	80.5	18.7	145.3	602	A
B1665x_XK	-22.82	27.23	SKK	39	9	0.75	0.1	272.7	14.0	-91.9	24	B
B1665x_XK	-22.82	27.23	SKK	63	17	0.55	0.22	81.7	18.7	145.3	602	B
B1665x_XK	-22.82	27.23	SKK	69	8.5	0.85	0.2	113.4	-6.6	155.1	56	B
B1665x_XK	-22.82	27.23	SKK	67	2	1.25	0.35	148.2	-24.6	179.1	527	B
B17CIx_XK	-19.29	22.91	SKK	23	6	1	0.22	42.2	49.8	145.1	583	B
B17CIx_XK	-19.29	22.91	SKK	31	9	1.05	0.27	56.8	37.9	143.9	31	B
SA65xx_XA	-22.82	27.22	SKK	41	17	0.5	0.28	74.9	23.9	141.9	95	B
SA65xx_XA	-22.82	27.22	SKK	46	10.5	1	0.25	273.2	14.4	-91.5	33	B
SA66xx_XA	-21.90	26.37	SKK	44	11.5	1	0.3	66.0	31.2	140.5	86	B
SA66xx_XA	-21.90	26.37	SKK	42	7	1.25	0.22	74.6	23.9	141.9	95	B
SA70xx_XA	-21.09	26.34	SKK	46	3	1.25	0.23	153.7	-32.1	179.8	332	B
SA70xx_XA	-21.09	26.34	SKK	29	5	1.7	0.25	65.5	31.2	140.5	86	B
SA70xx_XA	-21.09	26.34	SKK	24	10	1.3	0.3	74.1	23.9	141.9	95	B
SA70xx_XA	-21.09	26.34	SKK	41	3.5	1.4	0.28	146.9	-22.5	179.1	611	B

BIBLIOGRAPHY

Adam, J. M. C., and S. Lebedev (2012), Azimuthal anisotropy beneath southern Africa from very broad-band surface-wave dispersion measurements, Geophys. J. Int., 191, 155-174, doi:10.1111/j.1365-246X.2012.05583.x.

Alsina, D., and R. Snieder (1995), Small-scale sublithospheric continental mantle deformation: Constraints from SKS splitting observations, Geophys. J. Int., 123, 431-448, doi: 10.1111/j.1365-246X.1995.tb06864.x.

Altamimi, Z., X. Collilieux, and L. Metivier (2011), ITRF2008: An improved solution of the international terrestrial reference frame, J. Geodesy, 85, 457-473, doi:10.1007/s00190-011-0444-4.

Ammon, C. J. (1991), The isolation of receiver effects from teleseismic P-waveforms, Bull. Seismol. Soc. Am., 81, 2504–2510.

Anandakrishnan, S., and J. P. Winberry (2004), Antarctic subglacial sedimentary layer thickness from receiver function analysis, Global Planet. Change, 42, 167-176, doi:10.1016/j.gloplacha.2003.10.005.

Bagley, B., and A. A. Nyblade (2013), Seismic anisotropy in eastern Africa, mantle flow, and the African superplume, Geophys. Res. Lett., 40, 1500–1505, doi:10.1002/grl.50315.

Barruol, G., and W. B. Ismail (2001), Upper mantle anisotropy beneath the African IRIS and Geoscope stations, Geophys. J. Int., 146, 549-561, doi:10.1046/j.0956-540x.2001.01481.x.

Bashir, L., S. S. Gao, K. H. Liu, and K. Mickus (2011), Crustal structure and evolution beneath the Colorado Plateau and the southern Basin and Range Province: Results from receiver function and gravity studies, Geochem. Geophys. Geosyst., 12, Q06008, doi:10.1029/2011GC003563.

Begg, G. C., W. L. Griffin, L. M. Natapov, S. Y. O'Reilly, S. P. Grand, C. J. O'Neill, J. M. A. Hronsky, Y. Poudjom Djomani, C. J. Swain, T. Deen, and P. Bowden (2009), The lithospheric architecture of Africa: Seismic tomography, mantle petrology, and tectonic evolution, Geosphere, 5, 23-50, doi:10.1130/GES00179.1.

Bina, C. R., and G. Helffrich (1994), Phase transition Clapeyron slopes and transition zone seismic discontinuity topography, J. Geophys. Res., 99, 15,853–15,860, doi:10.1029/94JB00462.

Birt, C. S., P. K. H. Maguire, M. A. Khan, H. Thybo, G. R. Keller, and J. Patel (1997), The influence of pre-existing structures on the evolution of the southern Kenya Rift Valley-evidence from seismic and gravity studies, Tectonophysics, 278, 211–242, doi:10.1016/S0040-1951(97)00105-4.

Bostock, M. G., and A. M. Trehu (2012), Wave-Field Decomposition of Ocean Bottom Seismograms, Bull. Seism. Soc. Am., 102, 1,681-1,692, doi:10.1785/0120110162.

Bufford, K. M., E. A. Atekwana, M. G. Abdelsalam, E. Shemang, E. Atekwana, K. Mickus, M. Moidaki, M. P. Modisi, and L. Molwalefhe (2012), Geometry and faults tectonic activity of the Okavango Rift Zone, Botswana: Evidence from magnetotelluric and electrical resistivity tomography imaging, J. Afr. Earth. Sci., 65, 61-71, doi: 10.1016/j.jafrearsci.2012.01.004.

Burdick, L. J., and C. A. Langston (1977), Modeling crustal structure through the use of converted phases in teleseismic body-wave forms, Bull. Seism. Soc. Am., 67, 677-691.

Chevrot, S., and R. D. Van der Hilst (2000), The Poisson's ratio of the Australian crust: geological and geophysical implications, Earth Planet. Sci. Lett., 183, 121-132, doi: 10.1016/S0012-821X(00)00264-8.

Clitheroe, G., O. Gudmundsson, and B. L. N. Kennett (2000), Sedimentary and upper crustal structure of Australia from receiver functions, Austr. J. Earth Sci., 47, 209-216.

Conrad, C. P., and C. Lithgow-Bertelloni (2006), Influence of continental roots and asthenosphere on plate-mantle coupling, Geophys. Res. Lett., 33, L05312, doi:10.1029/2005GL025621.

Crampin, S. (1981), A review of wave motion in anisotropic and cracked elastic-media, Wave Motion, 3, 343-391, doi:10.1016/0165-2125(81)90026-3.

Daly, M. C., J. Chorowicz, and J. D. Fairhead (1989), Rift basin evolution in Africa: The influence of reactivated steep basement shear zones, Geol. Soc. Spec. Pub., 44, 309-334, doi:10.1144/GSL.SP.1989.044.01.17.

DeMets, C., R. G. Gordon, D. F. Argus, and S. Stein (1994), Effect of recent revisions to the geomagnetic reversal time scale on estimates of current plate motions, Geophys. Res. Lett., 21, 2191-2194, doi: 10.1029/94GL02118.

Doglioni, C. (1993), Geological evidence for a global tectonic polarity, J. Geol. Soc. London, 150, 991-1002, doi:10.1144/gsjgs.150.5.0991.

Ebinger, C. J., M. J. Crow, B. R. Rosendahl, D. A. Livingstone, and J. LeFournier (1984), Structural evolution of the Malawi rift, Africa, Nature, 308, 627-629, doi:10.1038/308627a0.

Efron, B., R. Tibshirani (1986), Bootstrap methods for standard errors, confidence intervals, and other measures of statistical accuracy, Stat. Sci., 1, 54–75, doi:10.1214/ss/1177013815.

Elsheikh, A. A., S. S. Gao, K. H. Liu, A. A. Mohamed, Y. Yu, and R. E. Fat-Helbary (2014), Seismic anisotropy and subduction-induced mantle fabrics beneath the Arabian and Nubian Plates adjacent to the Red Sea, Geophys. Res. Lett., 41, 2376–2381, doi:10.1002/2014GL059536.

Feng, Z., C. Jia, X. Xie, S. Zhang, Z. Feng, and T. A. Cross (2010), Tectonostratigraphic units and stratigraphic sequences of the nonmarine Songliao basin, northeast China, Basin Research, 22, 79-95, doi: 10.1111/j.1365-2117.2009.00445.x.

Fouch, M. J., K. Fischer, E. M. Parmentier, M. E. Wysession, and T. J. Clarke (2000), Shear-wave splitting, continental keels, and patterns of mantle flow, J. Geophys. Res., 105, 6255-6275, doi:10.1029/1999JB900372.

Gao, S., P. M. Davis, H. Liu, P. D. Slack, Y. A. Zorin, V. V. Mordvinova, V. M. Kozhevnikov, and R. P. Meyer (1994), Seismic anisotropy and mantle flow beneath the Baikal rift zone, Nature, 371, 149-151, doi:10.1038/371149a0.

Gao, S., P. M. Davis, H. Liu, P. D. Slack, A. W. Rigor, Y. A. Zorin, V. V. Mordvinova, V. M. Kozhevnikov, and N. A. Logatchev (1997), SKS splitting beneath continental rift zones, J. Geophys. Res., 102(B10), 22781–22797, doi:10.1029/97JB01858.

Gao, S. S., and K. H. Liu (2014a), Imaging mantle discontinuities using multiply-reflected P-to-S conversions, Earth Planet. Sci. Lett., 402, 99–106, doi:10.1016/j.epsl.2013.08.025.

Gao, S. S., and K. H. Liu (2014b), Mantle transition zone discontinuities beneath the contiguous United States, J. Geophys. Res., 119, 6,452–6,468, doi:10.1002/2014JB011253.

Gao, S. S., K. H. Liu, and M. G. Abdelsalam (2010), Seismic anisotropy beneath the Afar Depression and adjacent areas: Implications for mantle flow, J. Geophys. Res., 115, B12330, doi:10.1029/2009JB007141.

Gao, S. S., K. H. Liu, P. M. Davis, P. D. Slack, Y. A. Zorin, V. V. Mordvinova, and V. M. Kozhevnikov (2003), Evidence for small-scale mantle convection in the upper mantle beneath the Baikal rift zone, J. Geophys. Res., 108, 2194, doi:10.1029/2002JB002039.

Gao, S. S., K. H. Liu, C. A. Reed, Y. Yu, B. Massinque, H. Mdala, M. Moidaki, D. Mutamina, E. A. Atekwana, S. Ingate, and A. M. Reusch (2013), Seismic Arrays to Study African Rift Initiation, Eos Trans. AGU, 94, 213, doi: 10.1002/2013EO240002.

Gao, S. S., P. G. Silver, K. H. Liu, and the Kaapvaal Seismic Group (2002), Mantle discontinuities beneath Southern Africa, Geophys. Res. Lett., 29, 1,291-1,294, doi:10.1029/2001GL013834.

Gashawbeza, E. M., S. L. Klemperer, A. A. Nyblade, K. T. Walker, and K. M. Keranen (2004), Shear-wave splitting in Ethiopia: Precambrian mantle anisotropy locally modified by Neogene rifting, Geophys. Res. Lett., 31, L18602, doi:10.1029/2004GL020471.

Gripp, A. E., R. G. Gordon (2002), Young tracks of hotspots and current plate velocities, Geophys. J. Int., 150, 321-361, doi:10.1046/j.1365-246X.2002.01627.x.

Gung, Y., M. Panning, and B. Romanowicz (2003), Global anisotropy and the thickness of continents, Nature, 422, 707?711, doi:10.1038/nature01559.

Hanson, R. E. (2003). Proterozoic geochronology and tectonic evolution of southern Africa, Geol. Soc. Spec. Pub., 206, 427-463, doi:10.1144/GSL.SP.2003.206.01.20.

He, C., S. Dong, and X. Chen (2012), Seismic technique for studying sedimentary layer: Bohai Basin as an example, Acta Geologica Sinica, 86, 1,105-1,115, doi:10.1111/j.1755-6724.2012.00734.x.

Hill, R. I. (1991), Starting plumes and continental break-up, Earth Planet. Sci. Lett., 104, 398-416, doi:10.1016/0012-821X(91)90218-7.

Huerta, A. D., A. A. Nyblade, and A. M. Reusch (2009), Mantle transition zone structure beneath Kenya and Tanzania: more evidence for a deep-seated thermal upwelling in the mantle, Geophys. J. Int., 177, 1249–1255, doi:10.1111/j.1365-246X.2009.04092.x.

James, D. E., M. J. Fouch, J. C. VanDecar, and S. Van Der Lee (2001), Tectospheric structure beneath southern Africa, Geophys. Res. Lett., 28, 2,485-2,488, doi:10.1029/2000GL012578.

Karato, S. I., H. Jung, I. Katayama, and P. Skemer (2008), Geodynamic significance of seismic anisotropy of the upper mantle: new insights from laboratory studies, Annu. Rev. Earth Planet. Sci., 36, 59-95, doi:10.1146/annurev.earth.36.031207.124120.

Keller, G. R., M. A. Khan, P. Morgan, R. F. Wendlandt, W. S. Baldridge, K. H. Olsen, C. Prodehl, L. W. Braile (1991), A comparative study of the Rio Grande and Kenya rifts, Tectonophysics}, 197, 355-371, doi:10.1016/0040-1951(91)90050-3.

Kendall, J. M., S. Pilidou, D. Keir, I. D. Bastow, G. W. Stuart, and A. Ayele (2006), Mantle upwellings, melt migration, and the rifting of Africa: insights from seismic anisotropy. In: Yirgu, G., Ebinger, C.J., Maguire, P.K.H. (Eds.), The Afar volcanic province within the East African rift system, SP259. Geol. Soc. Spec. Publ., pp. 55-72, doi:10.1016/j.epsl.2007.09.038.

Khoza, T. D., A. G. Jones, M. R. Muller, R. L. Evans, M. P. Miensopust, and S. J. Webb (2013), Lithospheric structure of an Archean craton and adjacent mobile belt revealed from 2-D and 3-D inversion of magnetotelluric data: Example from southern Congo craton in northern Namibia, J. Geophys. Res., 118, 4,378–4,397, doi:10.1002/jgrb.50258.

Kinabo, B. D., J. P. Hogan, E. A. Atekwana, M. G. Abdelsalam, and M. P. Modisi (2008), Fault growth and propagation during incipient continental rifting: Insights from a combined aeromagnetic and Shuttle Radar Topography Mission digital elevation model investigation of the Okavango Rift Zone, northwest Botswana, Tectonics, 27, TC3013, doi:10.1029/2007TC002154.

King, S. D., and D. L. Anderson (1998), Edge-driven convection, Earth Planet. Sc. Lett., 160(3), 289-296, doi:10.1016/S0012-821X(98)00089-2.

Koch, F. W., D. A. Wiens, A. A. Nyblade, P. J. Shore, R. Tibi, B. Ateba, C. T. Tabod, and J. M. Nnange (2012), Upper-mantle anisotropy beneath the Cameroon Volcanic Line and Congo craton from shear wave splitting measurements, Geophys. J. Int., 190, 75-86, doi:10.1111/j.1365-246X.2012.05497.x.

Kreemer, C. (2009), Absolute plate motions constrained by shear wave splitting orientations with implications for hot spot motions and mantle flow, J. Geophys. Res., 114, B10405, doi:10.1029/2009JB006416.

Langston, C. A. (1979), Structure under Mount Rainier, Washington, inferred from teleseismic body waves, J. Geophys. Res., 84, 4,749-4,762, doi:10.1029/JB084iB09p04749.

Langston, C. A. (2011), Wave-field continuation and decomposition for passive seismic imaging under deep unconsolidated sediments, Bull. Seismol. Soc. Amer., 101, 2,176-2,190, doi:10.1785/0120100299.

Leahy, G. M., R. L. Saltzer, and J. Schmedes (2012), Imaging the shallow crust with teleseismic receiver functions, Geophys. J. Int., 191, 627-636, doi:10.1111/j.1365-246X.2012.05615.x.

Lemnifi, A. A., K. H. Liu, S. S. Gao, C. A. Reed, A. A. Elsheikh, Y. Yu, and A. A. Elmelade (2015), Azimuthal anisotropy beneath north central Africa from shear wave splitting analyses, Geochem. Geophys. Geosyst., 16, doi:10.1002/2014GC005706.

Leseane, K., E. A. Atekwana, K. L. Mickus, M. G. Abdelsalam, E. M. Shemang, and E. A. Atekwana (2015), Thermal perturbations beneath the incipient Okavango Rift Zone, northwest Botswana, J. Geophys. Res., 120, 1210-1228. doi: 10.1002/2014JB011029.

Litasov, K. D., E. Ohtani, A. Suzuki, and K. Funakoshi (2005), Wet subduction versus cold subduction, Geophys. Res. Lett., 32, L13312, doi:10.1029/2005GL022921.

Liu, K. H. (2009), NA-SWS-1.1: A uniform database of teleseismic shear-wave splitting measurements for North America, Geochem. Geophys. Geosyst., 10, Q05011, doi:10.1029/ 2009 GC002440.

Liu, K. H., A. Elsheikh, A. Lemnifi, U. Purevsuren, M. Ray, H. Refayee, B. Yang, Y. Yu, and S. S. Gao (2014), A uniform database of teleseismic shear wave splitting measurements for the western and central United States, Geochem. Geophys. Geosyst., 15, 2075–2085, doi:10.1002/2014GC005267.

Liu, K. H., and S.S. Gao (2006), Mantle transition zone discontinuities beneath the Baikal rift and adjacent areas, J. Geophys. Res., 111, B11301, doi:10.1029/2005JB004099.

Liu, K. H., and S. S. Gao (2010), Spatial variations of crustal characteristics beneath the Hoggar swell, Algeria, revealed by systematic analyses of receiver functions from a single seismic station, Geochem. Geophys. Geosyst., 11, Q08011, doi:10.1029/2010GC003091.

Liu, K. H., and S. S. Gao (2011), Estimation of the depth of anisotropy using spatial coherency of shear-wave splitting parameters, B. Seismol. Soc. Am., 101, 2153-2161, doi:10.1785/0120100258.

Liu, K. H., and S. S. Gao (2013), Making reliable shear-wave splitting measurements, Bull. Seismol. Soc. Am., 103, 2680-2693, doi: 10.1785/0120120355.

Liu, K. H., S. S. Gao, Y. Gao, and J. Wu (2008), Shear wave splitting and mantle flow associated with the deflected Pacific slab beneath northeast Asia, J. Geophys. Res., 113, B01305, doi:10.1029/2007JB005178.

Liu, K. H., S. S. Gao, P. G. Silver, and Y. Zhang (2003), Mantle layering across central South America, J. Geophys. Res., 108, 2510, doi:10.1029/2002JB002208.

Mandal, P. (2006), Sedimentary and crustal structure beneath Kachchh and Saurashtra regions, Gujarat, India, Phys. Earth Planet. Inter., 155, 286-299, doi:10.1016/j.pepi.2006.01.002.

Mainprice, D., G. Barruol, and W. B. IsmaÃ¯L (2000), The seismic anisotropy of the Earth's mantle: from single crystal to polycrystal, in Earth's Deep Interior: Mineral Physics and Tomography From the Atomic to the Global Scale (eds S.-I. Karato, A. Forte, R. Liebermann, G. Masters and L. Stixrude), AGU, Washington, D.C., doi:10.1029/GM117p0237.

Malservisi, R., U. Hugentobler, R. Wonnacott, and M. Hackl (2013), How rigid is a rigid plate? Geodetic constraint from the TrigNet CGPS network, South Africa, Geophys. J. Int., 192, 918-928, doi:10.1093/gji/ggs081.

McCourt, S., R. A. Armstrong, H. Jelsma, and R. B. M. Mapeo (2013), New U–Pb SHRIMP ages from the Lubango region, SW Angola: insights into the Palaeoproterozoic evolution of the Angolan Shield, southern Congo Craton, Africa, J. Geol. Soc. London, 170, 353-363, doi:10.1144/jgs2012-059.

Miensopust, M. P., A. G. Jones, M. R. Muller, X. Garcia, and R. L. Evans (2011), Lithospheric structures and precambrian terrane boundaries in northeastern Botswana revealed through magnetotelluric profiling as part of the southern African magnetotelluric experiment, J. Geophys. Res., 116, B02401, doi:10.1029/2010JB007740.

Miller, M. S., A. A. Allam, T. W. Becker, J. F. Di Leo, and J. Wookey (2013), Constraints on the tectonic evolution of the westernmost Mediterranean and northwestern Africa from shear wave splitting analysis, Earth Planet. Sc. Lett., 375, 234-243, doi:10.1016/j.epsl.2013.05.036.

Modisi, M. P., E. A. Atekwana, A. B. Kampunzu, T. H. Ngwisanyi (2000), Rift kinematics during the incipient stages of continental extension: evidence from the nascent Okavango rift basin, northwest Botswana, Geology, 28, 939–942, doi:10.1130/0091-7613(2000)28<939:RKDTIS>2.0.CO;2.

Mohamed, A. A., S. S. Gao, A. A. Elsheikh, K. H. Liu, Y. Yu, and R. E. Fat-Helbary (2014), Seismic imaging of mantle transition zone discontinuities beneath the northern Red Sea and adjacent areas, Geophys. J. Int., 199, 648-657, doi:10.1093/gji/ggu284.

Moore, W. R. (1985), Seismic profiles of the Powder River basin, Wyoming, in Seismic Exploration of the Rocky Mountain Region, edited by Griesand R. R. and Dyer R. C. Dyer, Rocky Mt. Assoc. of Geol., Denver, Colo., 187-200.

Mulibo, G. D., and A. A. Nyblade (2013), Mantle transition zone thinning beneath eastern Africa: Evidence for a whole-mantle superplume structure, Geophys. Res. Lett., 40, 3562–3566, doi:10.1002/grl.50694.

Muller, M. R., A. G. Jones, R. L. Evans, H. S. Grutter, C. Hatton, X. Garcia, M. P. Hamilton, M. P. Miensopust, P. Cole, T. Ngwisanyi, D. Hutchins, C. J. Fourie, H. A. Jelsma, S. F. Evans, T. Aravanis, W. Pettit, S. J. Webb, J. Wasborg, and The SAMTEX Team (2009), Lithospheric structure, evolution and diamond prospectivity of the Rehoboth Terrane and Western Kaapvaal Craton, Southern Africa: Constraints from broadband magnetotellurics, Lithos., 112, 93-105, doi:10.1016/j.lithos.2009.06.023.

Nair, S. K., S. S. Gao, K. H. Liu, and P. G. Silver (2006), Southern African crustal evolution and composition: Constraints from receiver function studies, J. Geophys. Res., 111, B02304, doi:10.1029/2005JB003802.

Niu, F., and J. Li (2011), Component azimuths of the CEArray stations estimated from P-wave particle motion, Earthquake Science, 24, 3-13, doi:10.1007/s11589-011-0764-8.

O'Neill, C. J., A. Kobussen, and A. Lenardic (2010), The mechanics of continental lithosphere-asthenosphere coupling, Lithos, 120, 55-62, doi:10.1016/j.lithos.2010.07.008.

Owens, T. J., G. Zandt, and S. R. Taylor (1984), Seismic evidence for an ancient rift beneath the Cumberland Plateau, Tennessee: A detailed analysis of broadband teleseismic P waveforms, J. Geophys. Res., 89, 7,783-7,795, doi:10.1029/JB089iB09p07783.

Prasad, M., M. A. Zimmer, P. A. Berge, and B. P. Bonner (2004), Laboratory measurements of velocity and attenuation in sediments, LLNL Rep. UCRL-JRNL-205155, 34 pp., Lawrence Livermore Natl. Lab., Livermore, Calif.

Press, W. H., S. A. Teukolsky, W. T. Vetterling, and B. P. Flannery (1992), Numerical Recipes in FORTRAN, second ed., Cambridge Univ. Press, Cambridge, U.K..

Randall, G. (1994), Efficient calculation of complete differential seismograms for laterally homogeneous earth models, Geophys. J. Int., 118, 245-254, doi:10.1111/j.1365-246X.1994.tb04687.x.

Reed, C. A., S. Almadani, S. S. Gao, A. Elsheikh, S. Cherie, M. Abdelsalam, A. Thurmond, and K. H. Liu (2014), Receiver function constraints on crustal seismic velocities and partial melting beneath the Red Sea rift and adjacent regions, Afar Depression, J. Geophys. Res., 119, 2,138-2,152, doi:10.1002/2013JB010719.

Reeves, C. V. (1972), Rifting in the Kalahari?, Nature, 237, 95–96, doi:10.1038/237095a0.

Refayee, H. A., B. B. Yang, K. H. Liu, and S. S. Gao (2014), Mantle flow and lithosphere?asthenosphere coupling beneath the southwestern edge of the North American craton: constraints from shear-wave splitting measurements, Earth Planet. Sc. Lett., 402, 209-220, doi:10.1016/j.epsl.2013.01.031.

Ritsema, J., S. Ni, D. V. Helmberger, and H. P. Crotwell (1998), Evidence for strong shear velocity reductions and velocity gradients in the lower mantle beneath Africa, Geophys. Res. Lett., 25, 4245-4248, doi:10.1029/1998GL900127.

Rychert, C. A., S. Rondenay, and K. M. Fischer (2007), P-to-S and S-to-P imaging of a sharp lithosphere-asthenosphere boundary beneath eastern North America, J. Geophys. Res., 112, B08314, doi:10.1029/2006JB004619.

Sandvol, E., J. Ni, S. Ozalaybey, and J. Schlue (1992), Shear-wave splitting in the Rio Grande Rift, Geophys. Res. Lett., 19, 2337-2340, doi:10.1029/92GL02715.

Sengör, A. M., and K. Burke (1978), Relative timing of rifting and volcanism on Earth and its tectonic implications, Geophys. Res. Lett., 5, 419-421, doi:10.1029/GL005i006p00419.

Sheehan, A. F., G. A. Abers, C. H. Jones, and A. L. Lerner-Lam (1995), Crustal thickness variations across the Colorado Rocky Mountains from teleseismic receiver functions, J. Geophys. Res., 100, 20,391-20,404, doi:10.1029/95JB01966.

Silver, P. G. (1996), Seismic anisotropy beneath the continents: Probing the depths of geology, Annu. Rev. Earth Planet. Sci., 24, 385-432.

Silver, P. G., and W. W. Chan (1991), Shear wave splitting and subcontinental mantle deformation, J. Geophys. Res., 96, 16,429-16,454.

Silver, P. G., S. S. Gao, K. H. Liu, and The Kaapvaal Seismic Group (2001), Mantle deformation beneath southern Africa, Geophys. Res. Lett., 28, 2493-2496, doi:10.1029/2000GL012696.

Silver, P. G., and M. Savage (1994), The interpretation of shear-wave splitting parameters in the presence of two anisotropic layers, Geophys. J. Int., 119, 949-963, doi:10.1111/j.1365-246X.1994.tb04027.x.

Snelson, C. M., T. J. Henstock, G. R. Keller, K. C. Miller, and A. Levander (1998), Crustal and uppermost mantle structure along the Deep Probe seismic profile, Rocky Mountain Geology, 33, 181-198, doi:10.2113/33.2.181.

Stern, R. J. (1994), Arc assembly and continental collision in the Neoproterozoic East African Orogen: Implications for the consolidation of Gondwanaland, Annu. Rev. Earth Planet. Sci., 22, 319-351, doi:10.1146/annurev.ea.22.050194.001535.

Stoffa, P. L., P. Buhl, and G. Bryan (1974), The application of homomorphic deconvolution to shallow-water marine seismology-Part I: Models, Geophysics, 39, 401-416, doi: 10.1190/1.1440438.

Tao, K., T. Z. Liu, J. Y. Ning, and F. Niu (2014), Estimating sedimentary and crustal structure using wavefield continuation: theory, techniques and applications, Geophys. J. Int., 197, 443-457, doi:10.1093/gji/ggt515.

Thorwart, M., and T. Dahm (2005), Wavefield decomposition for passive ocean bottom seismological data, Geophys. J. Int., 163, 611-621, doi:10.1111/j.1365-246X.2005.02761.x.

Versfelt, J., and B. R. Rosendahl (1989), Relationships between pre-rift structure and rift architecture in Lakes Tanganyika and Malawi, East Africa, Nature, 337, 354-357, doi: 10.1038/337354a0.

Vinnik, L. P., R. W. E. Green, and L. O. Nicolaysen (1996), Seismic constraints on dynamics of the mantle of the Kaapvaal craton, Phys. Earth Planet. Int., 95, 139-151, doi:10.1016/0031-9201(95)03123-5.

Vinnik, L., S. Kiselev, M. Weber, S. Oreshin, and L. Makeyeva (2012), Frozen and active seismic anisotropy beneath southern Africa, Geophys. Res. Lett., 39, L08301, doi:10.1029/2012GL051326.

White, R., and D. McKenzie (1989), Magmatism at rift zones: The generation of volcanic continental margins and flood basalts, J. Geophys. Res., 94, 7685-7729, doi:10.1029/JB094iB06p07685.

Wilson, D., R. Aster, J. Ni, S. Grand, M. West, W. Gao, W. S. Baldridge, and S. Semken (2005), Imaging the seismic structure of the crust and upper mantle beneath the Great Plains, Rio Grande Rift, and Colorado Plateau using receiver functions, J. Geophys. Res., 110, B05306, doi:10.1029/2004JB003492.

Yang, B. B., S. S. Gao, K. H. Liu, A. A. Elsheikh, A. A. Lemnifi, H. A. Refayee, and Y. Yu (2014),Seismic anisotropy and mantle flow beneath the northern Great Plains of North America, J. Geophys. Res. Solid Earth, 119, 1971–1985, doi:10.1002/2013JB010561.

Yeck, W. L., A. F. Sheehan, and V. Schulte-Pelkum (2013), Sequential h-k stacking to obtain accurate crustal thicknesses beneath sedimentary basins, Bull. Seismol. Soc. Amer., 103, 2,142-2,150, doi:10.1785/0120120290.

Yilmaz, O. (2001), Seismic data analysis: processing, inversion and interpretation of seismic data, Soc. Explo. Geophysicists, Tulsa, OK.

Yu, Y., C. A. Reed, S. S. Gao, K. H. Liu, B. Massinque, H. Mdala, M. Moidaki, D. Mutamina, E. Atekwana, S. Ingate, M. Reusch, and N. Barstow (2013), Crustal and mantle structure and anisotropy beneath the incipient segments of the East African Rift System: Preliminary results from the ongoing SAFARI, AGU Fall Meet. Abstracts, 1, 2542.

Yu, Y., K. H. Liu, M. Moidaki, C. A. Reed, S. S. Gao (submitted), No thermal anomalies in the mantle transition zone beneath an incipient continental rift: Evidence from the first receiver function study across the Okavango Rift Zone, Botswana, Submitted.

Zandt, G., and C. J. Ammon (1995), Continental crust composition constrained by measurements of crustal Poisson's ratio, Nature, 374, 152-154, doi:10.1038/374152a0.

Zelt, B. C., and R. M. Ellis (1999), Receiver-function studies in the Trans-Hudson orogen, Saskatchewan, Can. J. Earth Sci., 36, 585-603.

Zhu, L., and H. Kanamori (2000), Moho depth variation in southern California from teleseismic receiver functions, J. Geophys. Res., 105, 2,969-2,980, doi:10.1029/1999JB900322.

Zuleta-Tobon, L. M. (2012), Near-surface characterization and Vp/Vs analysis of a shale gas basin, MS thesis, University of Calgary, http://hdl.handle.net/1880/48952.

VITA

Youqiang Yu was born in the city of Zibo, China. He received his Bachelor's degree in Applied Geophysics from China University of Petroleum (Huadong), sitting in the middle-east coast of China in May, 2011. He joined the PhD program in Geology and Geophysics at Missouri University of Science and Technology (Missouri S&T) in August, 2011.

During his graduate studies, he was actively involved in various academic activities. He was an active member in the American Geophysical Union (AGU), Society of Exploration Geophysics (SEG), American Association of Petroleum Geologist (AAPG), and Geologic Society of America (GSA). He presented his research works at the AGU annual meeting in 2013, 2014, and the south-central GSA meeting in 2015. He was fully responsible for the seismic station service and demobilization work in Botswana and has made 5 trips to Botswana, spending a total of 6 months in Africa. He was one of the five Missouri S&T team members to participate in the AAPG Imperial Barrel Award Program in 2014 and awarded as honorable mention. He was also one of the four Missouri S&T Puzzle team members to win first prize in the Ocean Academic Competition of North America organized by Schlumberger Company in 2015.

He received Doctor of Philosophy degree in August, 2015.